Shear-wave splitting around the Eifel hotspot: evidence for a mantle upwelling

K. T. Walker,[1,]* G. H. R. Bokelmann,[1,]† S. L. Klemperer[1] and G. Bock[2]‡

[1]*Department of Geophysics, Stanford University, Stanford, CA, 94305 USA. E-mail: walker@ucsd.edu*
[2]*GeoForschungsZentrum Potsdam, Telegrafenberg* E325, *D-14473, Potsdam, Germany*

SUMMARY
We present the results of a shear-wave splitting analysis across the Eifel hotspot in west-central Europe. Our data set includes 18 permanent European broadband stations and 102 temporary Eifel broadband and short-period stations. We observe variations in splitting at most permanent stations, but are not able to model them reliably with unique dipping-axis or two-layer anisotropy models. We prefer instead a single-layer model with a horizontal fast axis to approximate the first-order anisotropy, which varies smoothly between stations. We observe a first-order parabolic pattern in fast polarization azimuth around the hotspot, which suggests that a lattice preferred orientation (LPO) of olivine fast axes exists in the asthenosphere as a result of the interaction between the slowly WSW-moving Eurasian plate and a mantle upwelling beneath the Eifel volcanic fields. The minority of the variation not explained by this model correlates with rapid lateral changes in splitting, and is interpreted as a result of additional anisotropy and/or the effects of dynamic recrystallization associated with LPO development in the region of corner flow near the conduit. Our parabolic asthenospheric flow (PAF) interpretation is consistent with Eifel geological, tomographic, receiver function, global absolute plate motion, electrical conductivity anisotropy, and geochemical studies, as well as with splitting studies in the Great Basin and around Hawaii. We suggest that the Eifel upwelling is sporadic, and a result of a low excess upwelling temperature and/or varying crustal stresses that periodically shift and facilitate eruption. The PAF pattern we observe neither suggests nor rules out anisotropy in the conduit associated with a wet Eifel upwelling. We use our optimum PAF model parameters to calculate a Eurasian plate speed of 12 km Ma^{-1}, which is consistent with the recent HS3-NUVEL1A speed of 19 $\pm$ 14 km Ma^{-1}.

Key words: anisotropy, Eifel, hotspots, plumes, shear-wave splitting, upwellings.

1 INTRODUCTION

1.1 Hotspots and upwellings

Cylindrical conduits of upwelling mantle material beneath hotspots, often referred to as 'plumes', are elusive targets of investigation because of their narrow width and depth. Regional tomographic inversions of teleseismic body-wave data, which suffer from the inherent trade-off between misfit reduction and model complexity, tend to smear anomalies vertically in regions penetrated by mostly subvertical rays. Consequently, tomographic inversions beneath hotspots

(e.g. Wolfe *et al.* 2002) have led to intriguing, but controversial, images. In addition, resolution constraints in previous global and regional inversions have limited detailed imaging of the deeper lower mantle beneath hotspots, fuelling a debate about the depth of origin of upper mantle upwellings (Ritsema & Allen 2003).

Seismic velocity anisotropy in the upper mantle that is detected by teleseismic shear-wave splitting (separation of the shear wave in an anisotropic rock into two polarized waves travelling at different speeds) can be explained by a lattice preferred orientation (LPO) of olivine fast a-axes, due to either past or present mantle deformation that occurs at least partly via dislocation creep (Nicolas & Christensen 1987; Silver 1996). This interpretation has been made to explain correlations of fast polarization azimuths with absolute plate motion (APM), implying shear between the lithosphere and a passive asthenosphere (Vinnik *et al.* 1992; Bormann *et al.* 1996; Russo & Okal 1998; Wolfe & Solomon 1998). The mantle–plume hypothesis predicts that ascending plume material is deflected and sheared by the lithosphere. This prediction can be tested by analysing

teleseismic splitting observed in regions where additional anisotropy does not overly mask the asthenospheric signal. This prediction has already been shown to be consistent with splitting data in the Great Basin (Savage & Sheehan 2000; Walker *et al.* 2004a) and around the Hawaiian hotspot (Walker *et al.* 2001, 2003; Vinnik *et al.* 2003).

In this paper, we analyse and model the splitting of teleseismic waveforms recorded by permanent and temporary seismic stations across the Eifel hotspot in Western Germany and the surrounding region. The Eifel data are anomalous when compared with those from the surrounding region, and allow us to put new constraints and inferences on the origin of anisotropy and the relationship between tectonics, magmatism, and geodynamics beneath west-central Europe. We show that, beneath the Eifel hotspot, the average magnitude of the delay times and a first-order variation in the fast polarization azimuths are explained best by anisotropy in the asthenosphere (and perhaps lower lithosphere) associated with a plume-like upwelling. We also show that the minority of the variation not explained by the upwelling flow is associated with rapid lateral variations in splitting, and could be explained by additional, more complicated, anisotropy in the lithosphere, as well as by anisotropic complexity associated with dynamic recrystallization in regions of corner flow.

1.2 Tectonic history of west-central Europe

The basement of west-central Europe is dominated by the NE-trending Rhenohercynian and Saxothuringian terranes (Fig. 1) (Franke 1989). These terranes are separated by deep, laterally continuous fault zones that may represent tectonic sutures associated with the Late Palaeozoic Hercynian orogeny, which resulted from the closure of the Proto-Tethys ocean and collision of Gondwanaland (Africa) with northern Europe. During the Cenozoic, a rift system developed across these structures from the North Sea to the Mediterranean (Ziegler 1992), of which the most prominent feature is the Rhine graben. It started rifting in the early Tertiary, and has experienced as much as 7 km of extension (Sittler 1969; Laubscher 1970; Doebl & Teichmüller 1979). West-central Europe has experienced minor magmatism in many areas since the late Oligocene, involving predominantly primitive alkalic magmas that appear to be spatially and temporally correlated with domal uplift of Hercynian basement massifs, and/or the development of the Cenozoic rift system (Ziegler 1992; Wilson & Patterson 2001). Geochemical studies suggest that this magmatism results either from partial melting of a primitive European asthenospheric reservoir located at the base of the upper mantle, in some places contaminated by partial melt of enriched lithospheric sources (Wilson & Patterson 2001), or from a source at the base of the lithosphere (Wilson & Downes 1992).

The Rhenish Massif, a ∼300-m domal Hercynian-basement uplift located at the junction of the Rhine, Leine, and Rur grabens, is onlapped by younger sedimentary sequences. This uplift began in the early Miocene, 20–40 Ma after the onset of Rhine-graben rifting. Although minor volcanism predated the onset of uplift in some places, the main phase of volcanism in the Rhenish Massif began during the same time as the uplift, but shifted to the Eifel volcanic fields west of the Rhine in the Quaternary (Fig. 1), where the most recent eruption was 11 000 years ago (Lippolt 1983; Mertes & Schmidt 1983). The Rhenish Massif continues to uplift with a maximum rate in the Eifel of 0.4–1 mm a^{-1} (Campbell *et al.* 2002). The current orientations of maximum horizontal compressive stress vary from Western Europe to Eastern Europe in roughly a fan-like pattern radiating from the Alps (Grünthal & Stromeyer 1992), which suggests that the Alps have been a source of intraplate compression.

A correlation has been argued to exist between the timing of magmatic activity and changes in the regional stress field, suggesting that the main volcanic phases are associated with periods of compressional stress relaxation in the foreland of the Alpine orogenic belt (Wilson & Bianchini 1999).

The uplift of the Rhenish Massif is probably related to recent mantle lithospheric thinning beneath it (Ziegler 1992). It is unclear, however, whether the uplift is due to (1) erosion of the lithosphere by buoyant upwelling mantle material, or (2) underplating of the crust associated with the upward percolation of partial melt through the thinned lithosphere (Turcotte & Emerman 1983; Wilson & Downes 1992). The uplift is probably not due to rifting alone, because such rifting should affect the topography of the entire length of the rift in the same fashion since the pre-existing regional structure is fairly consistent throughout the area. Rather, this uplift suggests a mantle hotspot beneath it, and the question becomes, what is the source of heat for this hotspot? If an upwelling is the source, either (1) it is a recent Quaternary upwelling, which explains the lack of an age progression of volcanic centres, or (2) the upwelling rate and excess temperature of the upwelling are too sporadic and low to generate a large amount of partial melt and surface volcanism, and either the upwelling is not stationary in the traditional fixed hotspot reference frame or the plate motion has changed significantly throughout the last 28 Ma since the onset of Rhenish Massif volcanism.

Teleseismic studies conducted across the Eifel hotspot have found evidence for a mantle upwelling. Inversions of backazimuthal variations in traveltime residuals have imaged slow velocity anomalies down to at least 400 km depth. Ritter *et al.* (2001) imaged a ∼70-km wide columnar *P*-wave anomaly, oriented roughly vertically and having a lateral contrast of up to 2 per cent and a centre at roughly ∼50.0°N, 6.4°E. Keyser *et al.* (2002) imaged two slow 150-km wide columnar *S* anomalies, one 2–5 per cent anomaly centred at ∼50.3°N, 7.0°E between 0 and 170 km depth, and another 2–3 per cent anomaly centred at ∼50.0°N, 6.9°E between 240 and 400 km depth. Analysing the backazimuthal variations in *P*-wave amplitude, Meyer (2001) imaged a columnar attenuation anomaly (*Q*), with a decrease in attenuation between 150 and 250 km. The *P*, *S*, and *Q* anomalies are interpreted to represent an upwelling conduit, with the gap in the *S* anomaly arising from an increase in the shear modulus from (1) a progressive dehydration process in the upwelling material between 240 and 400 km from a pressure-dependent solubility of the hydrous components (i.e. water being released from the hydrous minerals in the surrounding rock), and/or (2) a fractional melting process in the 170–240 km gap, preferentially removing water with the upward-migrating melts (Keyser *et al.* 2002). Receiver functions also resolve a depression of the 410-km discontinuity, but no variations in the 660-km discontinuity are resolved (Grunewald *et al.* 2001). Receiver functions also provide evidence for a low-velocity body with 1 per cent partial melt 60–90 km beneath the Eifel (Budweg 2003).

Passier & Snieder (1996) inverted a suite of Rayleigh-wave dispersion curves and found an 8–14 per cent velocity contrast across Western Germany. The geometry of their slow anomalies varies considerably with depth, but a columnar, roughly vertical anomaly centred at ∼49.3°N, 7.6°E is apparent down to 200 km depth. A detailed comparison of tomographic images from body waves (Ritter *et al.* 2001; Keyser *et al.* 2002) and surface waves (Passier & Snieder 1996) is difficult, given the different types of illustrations contained in each publication. However, the centres of the columnar *P* and *S* anomalies appear to be displaced by ∼60 km. The horizontal diameters of the *P*- (∼70 km) and *S*-wave (∼150 km) anomalies are also significantly different. In addition, the surface-wave anomaly
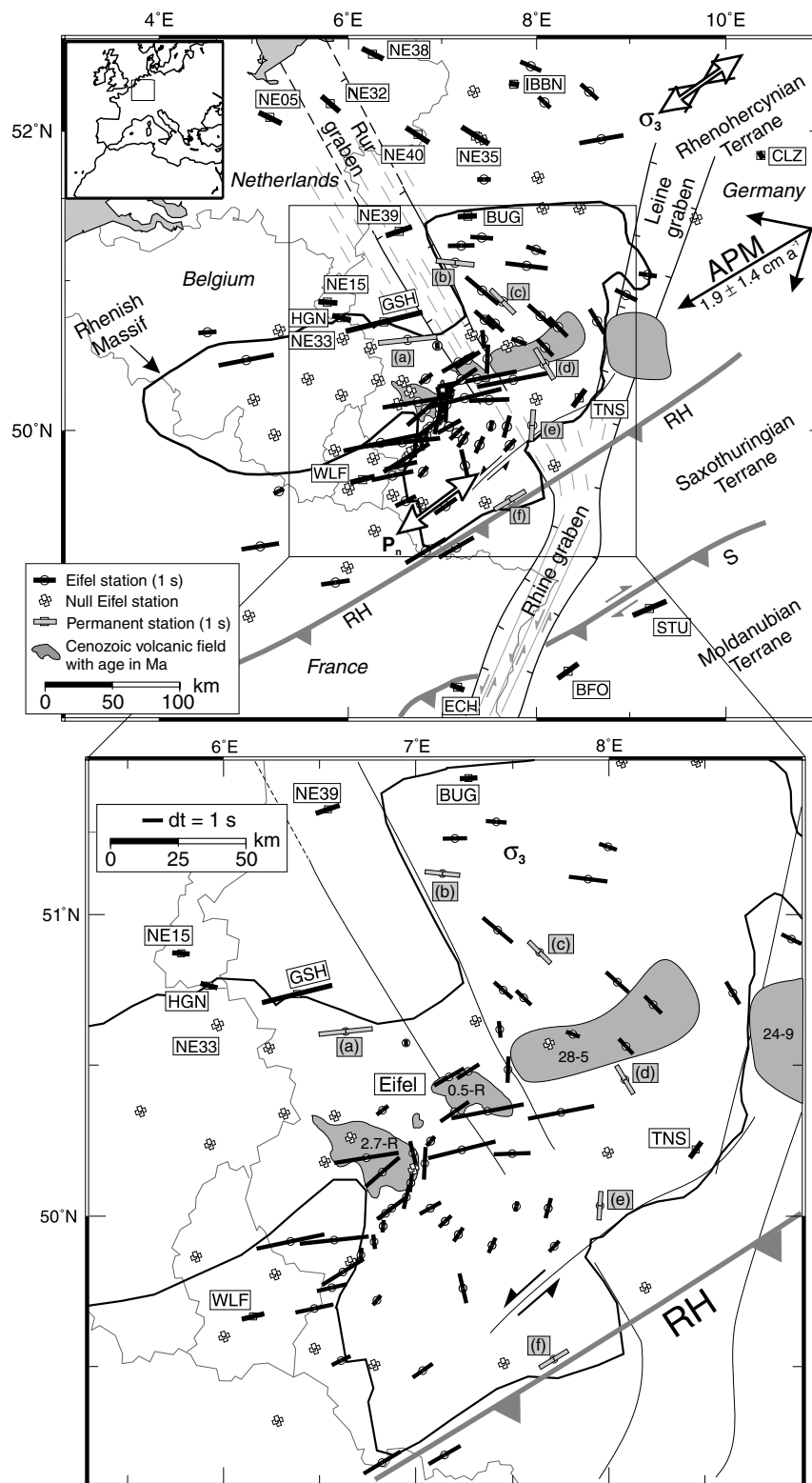
Figure 1. Eifel and surrounding region. Short bars: station shear-wave splitting estimates for Eifel (circles) and permanent stations (squares) with orientation parallel to the fast polarization azimuth and length parallel to delay time. Grey bars: Eifel station estimates in Fig. 8 (a–f). Thin lines: national boundaries. Thick grey lines: reverse and wrench faults that separate terranes that formed during the Hercynian orogeny (Edel & Fluck 1989): RH—Rhenohercynian and S—Saxothuringian sutures. Dark grey bodies: volcanic centres with their ages in Ma (R—Recent) (Illies *et al.* 1979; Jung & Hoernes 2000). Thick black lines: boundaries of uplifted Rhenish Massif. Black lines with hatch marks: Cenozoid rift system. Thin grey lines in the Rhine graben: left-lateral strike-slip faults (Edel & Fluck 1989). Short thin black lines in northern grabens: trends of anastomosing fault systems (Illies *et al.* 1979). Black vector in upper right: plate motion (and 2σ error bars) in a fixed hotspot reference frame (Gripp & Gordon 2002). Double-headed arrow in the south: P_n-velocity fast direction (Smith & Ekström 1999). Double-headed arrow in the north: orientation of regional least horizontal compressive stress (σ_3) (Mueller *et al.* 1997).

is ∼120 km distance from both the *P* and *S* teleseismic anomalies. The relative residual contrasts were up to 1.6 s for *P* (Ritter *et al.* 2001) and 6 s for *S* (Keyser *et al.* 2002). Spatial variations in anisotropy across the Rhenish Massif may help to explain these inconsistencies.

1.3 Deformation, anisotropy, and teleseismic shear-wave splitting

Olivine is a seismically anisotropic mineral that makes up a significant fraction of the upper mantle. It has a maximum *S*-wave seismic-velocity anisotropy of 12 per cent (Kumazawa & Anderson 1969). When an aggregate of olivine grains is deformed via dislocation creep, a fabric or lattice preferred orientation (LPO) develops where one or more of the three olivine crystallographic axes has a preferred orientation, leading to a bulk anisotropy for the aggregate (Nicolas & Christensen 1987). The orientation of the bulk anisotropy depends on which set of dislocation slip planes are active in accommodating the deformation, and what type of deformation is occurring (Nicolas & Poirier 1976; McKenzie 1979; Nicolas & Christensen 1987; Karato 1989; Ribe & Yu 1991; Ribe 1992). For progressive simple shear, the fast [100] a-axes of olivine rotate towards the orientation of shear. For uniaxial strain, the fast a-axes rotate away from the orientation of shortening, and towards the orientation of extension. Therefore, the fast orientation of the bulk anisotropy can be a proxy for mantle flow. A bulk anisotropy can also develop owing to a preferred orientation of structures such as cracks (Crampin 1991) or magma-filled lenses (Kendall 1994).

A teleseismic shear phase (plane wave) propagates through an anisotropic mantle as a pair of orthogonally polarized phases that travel at different speeds (e.g. Christensen 1966). The orientations of the polarization directions depend on the orientation of anisotropy with respect to the wave-front propagation direction. The delay time (*dt*) that accumulates between the two phases is proportional to the ray-path length and the magnitude of anisotropy sensed along the ray path. Typical shear-wave splitting analyses measure the horizontal projection of the fast polarization direction (fast polarization azimuth ϕ), and *dt* for several phases that propagate nearly vertically beneath the station. For a single anisotropic layer with a horizontal LPO of fast olivine a-axes, ϕ is horizontal and parallel to the fast a-axes, and *dt* is proportional to the layer thickness and magnitude of anisotropy. In the case of multiple anisotropic layers, splitting is still observed at the surface, and we refer to the measurements as 'apparent' splitting measurements. For a layer with a dipping fast axis (Savage 1998; Hartog & Schwartz 2000) or two sublayers of different anisotropy (Silver & Savage 1994), ϕ and *dt* will change in a predictable fashion as a function of initial polarization azimuth (IPA), backazimuth (BAZ), and incidence angle (INC). Therefore, apparent splitting measurements can yield important insights into the kinematics and magnitude of active and past deformation in the Earth's interior (Silver 1996).

1.4 Previous anisotropy studies in west-central Europe

There have been many previous shear-wave splitting studies beneath west-central Europe (Vinnik *et al.* 1989, 1992, 1994; Farra *et al.* 1991; Silver & Chan 1991; Bormann *et al.* 1993, 1996; Alsina & Snieder 1995; Brechner *et al.* 1998; Wylegalla *et al.* 1999). In the late 1980s, the number of waveforms available was quite limited, and single-layer models were estimated from the sparse data by default. With the advancements in the techniques to model split-

ting and with the availability of additional data, it appears that some stations in west-central Europe display variations in splitting parameters as a function of BAZ and/or IPA (Vinnik *et al.* 1994; Alsina & Snieder 1995; Brechner *et al.* 1998). In west-central through Eastern Europe, shear-wave splitting has been interpreted as resulting from fossilized anisotropy in the lithosphere associated with previous orogenies (Silver & Chan 1988; Vinnik *et al.* 1992; Bormann *et al.* 1993; Brechner *et al.* 1998), simple shear along the base of the plate associated with plate motion (Vinnik *et al.* 1989, 1994; Bormann *et al.* 1996; Brechner *et al.* 1998), and recent deformation of the lithospheric mantle associated with the Alpine orogeny (Vinnik *et al.* 1994; Brechner *et al.* 1998). The uncertainty exists in west-central and Central Europe because the Hercynian structural fabrics are approximately parallel to the Eurasian absolute plate motion in a fixed hotspot reference frame (Gripp & Gordon 2002), the strike of the Alpine orogenic belt, and the contours of the Moho topography, which have been argued as possible indicators of basal lithospheric topography (Bormann *et al.* 1996). In Eastern Europe, these Hercynian structures are not parallel to plate motion, or the Alps, but are parallel to the contours of the Moho topography, so the origin of anisotropy remains unclear.

P_n anisotropy studies throughout the region suggest a NNE–SSW fast orientation in the uppermost 5–10 km of mantle beneath the Moho (Hirn 1977; Fuchs 1977; Bamford 1977; Enderle *et al.* 1996). However, a recent global P_n anisotropy study found a NE–SW fast orientation (Fig. 1) (Smith & Ekström 1999). Observations of *P* delays across west-central Europe have been interpreted as evidence for a northwesterly dipping fast symmetry axis in the European lithosphere of the Saxothuringian and Rhenohercynian terranes (Babuška *et al.* 1984, 1993). In the Moldanubian terrane, the authors found evidence for a southeasterly dipping fast symmetry axis. A Rayleigh-wave azimuthal anisotropy study found a NE fast orientation in the Moldanubian terrane in South-Central Europe (Yanovskaya *et al.* 1990).

1.5 New broadband and short-period seismic data

From 1997 November to 1998 June, a network of 158 mobile short-period and broadband seismometers was deployed across the Eifel hotspot (Fig. 1). The objective of this large passive-source experiment was to investigate the nature of the mantle beneath the Eifel hotspot, searching for evidence for or against a plume origin (Ritter *et al.* 2000). We analyse and model the apparent splitting of *SKS* waveforms recorded by 102 of these seismic stations during the seven-month Eifel deployment.

Although the focus of our study is on the splitting beneath the Eifel Network, as a result of the paucity of data from the seven-month deployment, which prohibits us from testing between horizontal-axis, dipping-axis, and two-layer anisotropy models, we also made measurements on the permanent broadband stations in the surrounding region. As the duration of station recording increases, the ability of splitting analyses to characterize mantle anisotropy increases. These permanent stations have been recording for up to ∼15 yr, and therefore serve as references with which to compare results from the Eifel Network. For these stations, we analyse and model the splitting of core-refracted (*SKS*, *SKKS*, *PKS*) and direct *S* phases. Because the most recent west-central Europe permanent-station splitting study was published in 1998 (Brechner *et al.* 1998), we were able to process an additional five years of data.

In the following section, we describe our methodology, apply it to waveforms recorded by the permanent stations, and show that the
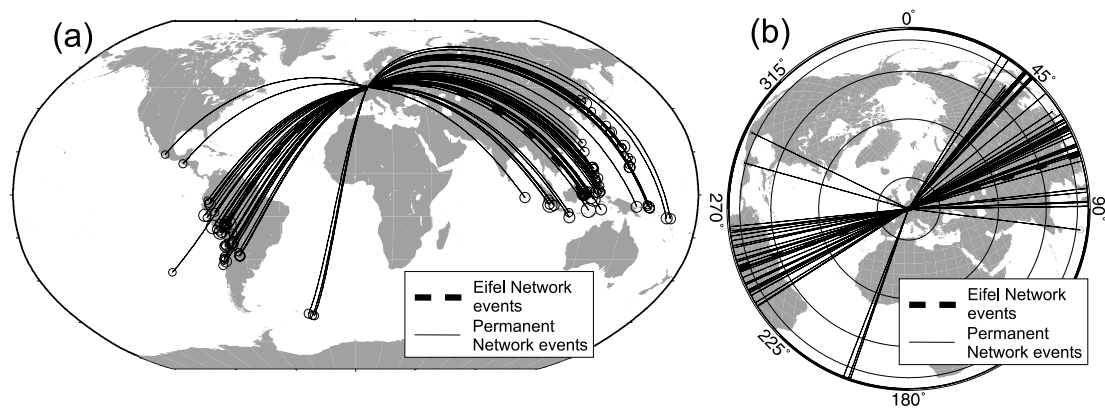
Figure 2. Distribution of the events analysed with energy SNR > 20. (a) shows the locations, whereas (b) shows the backazimuths in west-central Europe.

single-layer assumption explains the dominant source of anisotropy beneath most permanent stations. Because the permanent stations surround the Eifel region, and because we lack sufficient Eifel data to test more complex models, we extrapolate this single-layer model approach to the treatment of splitting across the Eifel Network.

2 METHODOLOGY TO MEASURE APPARENT SPLITTING

The delay time *dt* between fast and slow split waves is an integrated measure of anisotropy along the ray path, and cannot uniquely constrain the location of anisotropy, although we can infer the rough location by considering the origin of the initial polarization and surface-wave anisotropy studies. Core-refracted phases travel through the outer core as compressional phases and acquire their radial initial polarization during a *P*-to-*S* conversion at the core–mantle boundary (CMB) when they exit the core. Splitting of these phases must therefore be derived from anisotropy along the ray path from the CMB piercing point to the seismic station. The direct *S* phases obtain their initial polarization at the source. The strongest anisotropy observed by surface waves occurs between 50 and 300 km depth (Montagner 1994; Montagner & Guillot 2000). The best agreement on a global scale between measurements of splitting and surface-wave anisotropy occurs between 80 and 200 km depth (Montagner *et al.* 2000). The primary location of splitting is probably in this depth range. We are only interested in anisotropy beneath the seismic station, and we therefore reduce the possibility of source-side splitting by analysing direct *S* events only from hypocentres deeper than 300 km.

To make apparent splitting measurements, we use the method of Silver & Chan (1991) as modified by Walker *et al.* (2004b) to average out the instability associated with analysing slightly different time windows. Prior to analysis, the data are filtered with a zero-phase, four-pole bandpass filter from 5 to 50 s to maximize the signal-to-noise ratio (SNR). To restrict our analysis to good-quality data, we only analyse signals with energy SNR >20.

3 RESULTS

In this section, we present our shear-wave splitting results for the permanent and Eifel networks. We show that the splitting variations observed at most of the permanent stations cannot be reliably modelled by dipping-axis or two-layer anisotropy models, and argue that the most tectonically significant anisotropy model is that of a single

layer with a horizontal fast axis. We then treat splitting across the Eifel hotspot in the same fashion, and describe the spatial variations in the single-layer anisotropy models across the hotspot.

3.1 Permanent-station splitting measurements

3.1.1 General data description

We analyse 131 phases recorded on at least one of the stations, for a total of 358 analysed seismograms: *SKS* (305), *PKS* (21), *SKKS* (14), direct *S* (11), *sSKS* (4), and *pSKS* (3) phases (Fig. 2; Table S1). Most of the stations recorded a subset of these events, so BAZ coverage varies greatly. All analysed phases have steeply dipping INCs of ∼5°–30°, and sample the upper mantle almost directly beneath the station, providing very good lateral resolution. For the stations with the most recorded events (e.g. BFO, BUG, STU), the coverage in BAZ, IPA, and INC is not ideal, but is probably sufficient to discriminate between splitting from a single-layer model with a horizontal fast axis and that from a two-layer model with horizontal fast axes. For only these stations, the range of INC is probably sufficient to resolve dipping fast-axis models for a wide range of geometries.

Many of the phases we analysed did not demonstrate reliable apparent splitting, and yielded unconstrained measurements. Lack of apparent splitting can occur for a variety of reasons:

   (1) the Earth beneath the station is isotropic;
   (2) simple anisotropy exists and the IPA is parallel or perpendicular to the fast axis (often referred to as a 'null' measurement);
   (3) complex anisotropy exists and destructive interference occurs between multiply split phases or creates a complicated waveform that is not explained well by the optimum apparent splitting parameters;
   (4) the signal does not contain an adequate bandwidth to constrain the confidence region; or
   (5) the SNR is too low.

Our strict SNR threshold effectively eliminates (5) as a possibility, and we keep all the unconstrained measurements and refer to them as UCONS (Fig. 3).

3.1.2 Variations as a function of backazimuth (BAZ) and incidence angle (INC)

A single layer of anisotropy with a horizontal fast axis (HA model) gives rise to minor variations in splitting for INC < 30°. Conversely,
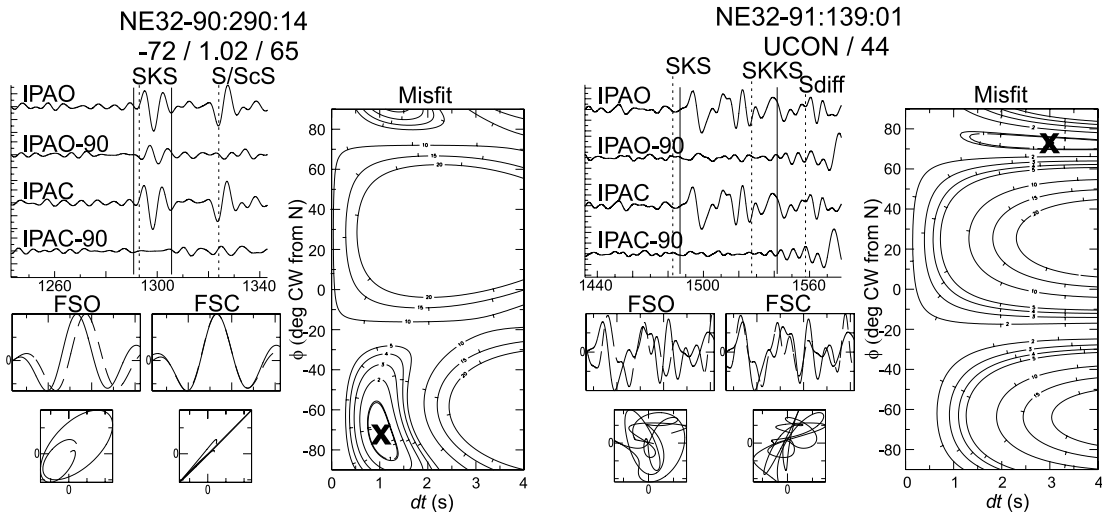
Figure 3. Examples of shear-wave splitting. Upper left: initial polarization azimuth and orthogonal complement of the original waveforms (IPAO, IPAO$-90°$) and anisotropy-corrected waveforms (IPAC, IPAC$-90°$). Dashed lines: IASP91 predicted phase arrival times. Vertical solid lines: picked time window. No energy should remain on the IPAC$-90°$ component if the splitting parameters predict the splitting. Lower right: fast/slow waves and corresponding horizontal particle motion. The misfit grid shows the minimum and 95 per cent confidence region corresponding to the optimum fast polarization azimuth (ϕ) and delay time (dt) that minimizes the energy on the IPAC$-90°$ component. The title indicates the station and event analysed (star-year:julday:hour), and the optimum parameters with signal-to-noise ratio (ϕ/dt/SNR). The event on the right is unconstrained (UCON) because its confidence region is truncated by the search grid.

variations as a function of BAZ and INC at a single station can arise from anisotropy that varies laterally across the station Fresnel zone, or from a single anisotropic layer with a dipping fast axis. It is difficult to distinguish between the two, but if fossilized anisotropy associated with vertically coherent deformation is the dominant mechanism, then we should observe spatial variations in the regional geological structures that correlate with variations in apparent splitting.

Many stations show locally consistent splitting. Fig. 4 shows polar plots of the apparent splitting as a function of BAZ and INC. In the Netherlands and northwest Germany, splitting is laterally consistent with ESE-SE ϕ and $dt \approx 1.0$ s. This changes in western Germany at NE39 and BUG, with NE-E ϕ. These observations are consistent with those found for the Netherlands stations by Alsina & Snieder (1995). However, most of the observed splitting at HS53, a composite of events from nearby stations NE15, NE33, GSH, and HGN (Fig. 1), is also fairly consistent with ESE ϕ. At STU, east of the Rhine graben, splitting is consistent with ENE ϕ and a longer dt ($\sim$1.5 s).

We observe significant variations in apparent splitting at other stations. Stations ECH and BFO show an interesting pattern that suggests that there is weak HA anisotropy (UCONS and short dt) beneath the Rhine graben, and that ϕ is subparallel to the graben strike. Splitting at CLZ is enigmatic, and it shows a strong directional dependence, with NNW ϕ from westerly BAZ, and NE ϕ from near-vertical INC and easterly BAZ. In addition, a cluster of UCONS exists for events from NE BAZ with greater INC.

Other stations have less pronounced variations. Events at WLF from NE BAZ have NE-ENE ϕ, whereas events from west BAZ have E ϕ. At IBBN, ϕ may rotate from NW for E BAZ to ENE for NNE BAZ. HS53 records no splitting for many events from WSW BAZ. A tight cluster of UCONS also exists for events from WSW BAZ at station IBBN.

Individual splitting at some stations for phases with similar BAZ and INC have different ϕ and/or dt (WLF, BUG, ECH, BFO), which

is inconsistent with a DA- or laterally varying HA-anisotropy model. Splitting beneath station WLF, may have a frequency dependence on splitting.

3.1.3 Dipping-axis (DA) modelling

We model the splitting for DA models at all stations for which an adequate number of data exist by assuming that the anisotropy beneath the station is uniform within the station Fresnel zone at all depths, and that it can be predicted from either an olivine elasticity tensor (orthorhombic symmetry; Kumazawa & Anderson 1969) or an oriented elasticity tensor averaged from petrofabric measurements on South African mafic kimberlite nodules (monoclinic symmetry for ϕ; Mainprice & Silver 1993). We perform a grid search over the tensor rotation angles that best explain the variation in splitting, and defer the details of this approach to Walker *et al.* (2004b). Because our assumed models of anisotropy require testing against different quantities of data at each station, there is a bias if we rely on a standard misfit reduction R to compare fits. To account for this, we use an adjusted R,

$$R^* = 1 - \frac{N-1}{N-k-1}(1-R), \tag{1}$$

where N is the number of data and k is the number of model parameters (Mendenhall & Sincich 1995). This value ranges from $-\infty$ to 1.0, and approaches R as N goes to ∞. We consider models that fit the data with $R^* > 0.25$ to be statistically significant (i.e. the model explains >25 per cent of the variation).

In this section, we determine the uniqueness of the optimum model in predicting the data by counting the number of minima in each misfit grid. We then determine which of these local minima fall below the 95 per cent confidence contour, and are therefore possible solutions. The best DA-model fit is provided by the kimberlite-nodule elasticity for HS53 ($R^* = 0.63$). This model yields four possible solutions out of the total of five minima for this station.
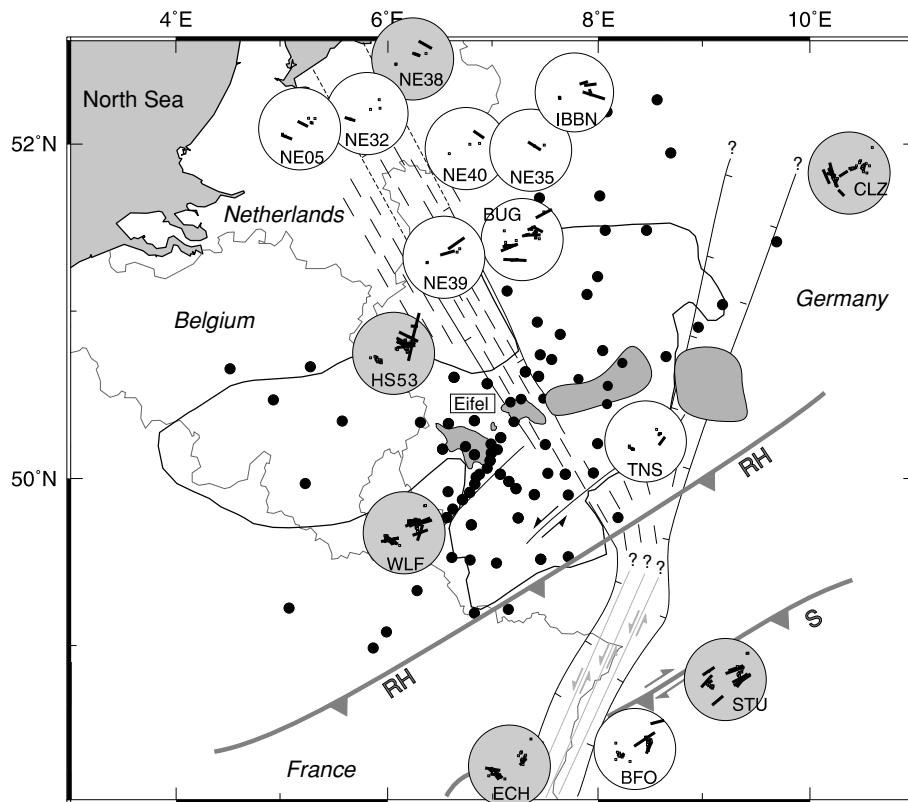
Figure 4. Polar plots of splitting measurements as a function of backazimuth (angle) and incidence angle (radius; max = 30°). Lines represent constrained splitting measurement with the orientation parallel to the fast polarization azimuth and the length proportional to delay time. Unconstrained measurements (UNCONS) are indicated by squares. Grey backgrounds indicate stations for which splitting can be explained by a dipping-axis anisotropy model(s) (Fig. 7). HS53 is a composite of data from stations GSH, HGN, NE15, and NE33 (Fig. 1).

As an example of the model fit for $R^* > 0.25$, Fig. 5 shows the best olivine and nodule DA models for HS53 and station ECH. Although at each station the model orientation parameters for olivine and nodule elasticities are similar, the patterns of predicted splitting are quite different owing to the differences in symmetry and magnitude of anisotropy for the tensors used in the two models. In addition, the thicknesses required to explain the dt are quite different for the olivine and nodule elasticities. For example, the olivine and nodule models for HS53 require thicknesses of 670 km and 1260 km. The relative thickness difference for the olivine and nodule models at ECH is even more extreme (145 km versus 770 km). Both models numerically fit the variation with some degree of success, but neither perfectly. We compare these models further in the model comparison section.

3.1.4 Variations as a function of initial polarization azimuth (IPA)

For vertically incident shear waves, Silver & Savage (1994) showed that two stacked horizontal layers of anisotropy with horizontal fast directions lead to a predictable variation in splitting with 90° periodicity in IPA. Rümpker & Silver (1998) showed that such variations also occur for relatively long-period signals ($T/dt \geq 5$) passing through a medium with a smoothly varying anisotropy from one fast direction at the bottom to another at the top. The dominant period T of our teleseismic signals is $\sim$10 s, and thus our data fit this criterion for dt up to 2.0 s. If a simple two-layer (TL) or smoothly varying anisotropy exists, we should be able to detect it for stations with good IPA coverage.

Fig. 6 shows plots of the apparent splitting measurements versus IPA for all stations with more than one constrained splitting measurement. Station IBBN shows an increasing ϕ with increasing IPA. However, the error bars are large enough to permit a single ϕ and dt to explain all the data. Station BFO appears to show a significant trend in both ϕ and dt. This trend may be explained better, however, by the laterally varying anisotropy that is suggested when comparing the splitting observed at stations ECH, BFO, and STU (Fig. 4).

Outliers were observed at HS53 and ECH. If taken literally, these measurements would require anisotropic complexity beneath the stations, that is, a more complicated model than a HA model. Furthermore, UCONS occur for a wide range of IPA at stations BFO, BUG, CLZ, ECH, HS53 and WLF, suggesting complexity beneath these stations. STU, however, has UCONS only for an IPA of $\sim$70°.

3.1.5 Two-layer (TL) modelling

We use the apparent-splitting analytical expressions derived by Silver & Savage (1994) and perform a grid search over the four trial parameters (ϕ and dt for the upper and lower layers) to determine the optimum two-layer (TL) anisotropy model with horizontal fast axes for a dominant signal period of 10 s. The thicknesses of these layers cannot be uniquely determined, but dt is proportional to the layer thickness and per cent anisotropy.

We used two different data sets in this modelling: constrained measurements with UCONS (YUCONS) and constrained measurements without UCONS (NUCONS). Silver & Savage (1994) showed
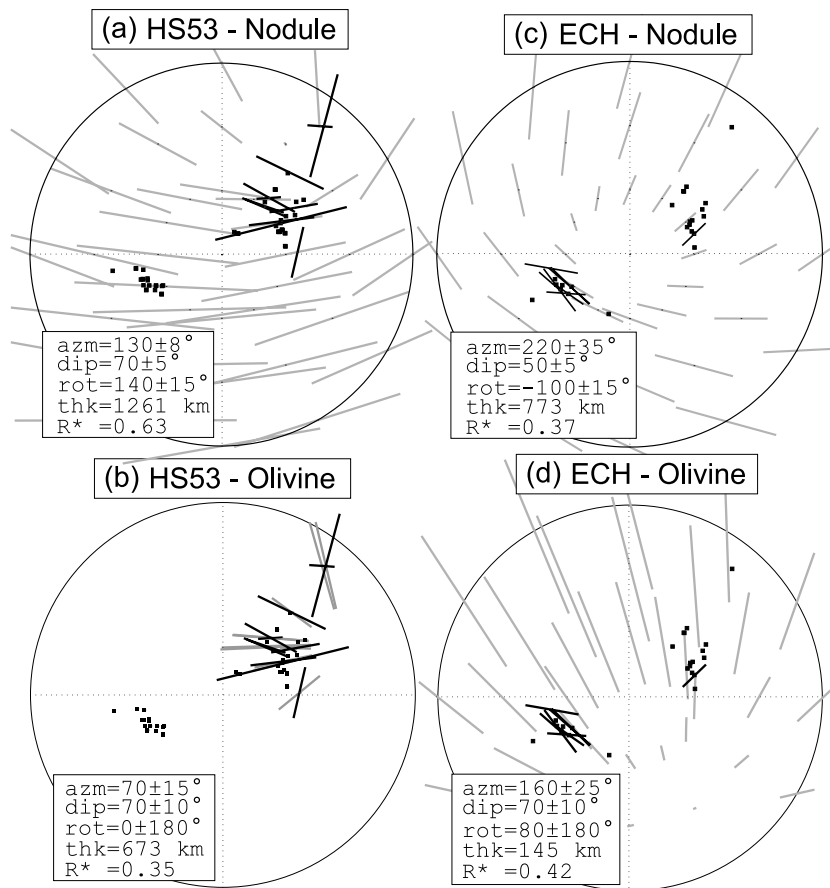
Figure 5. Polar plots showing examples of predicted splitting for a dipping-axis olivine and nodule anisotropy model beneath stations HS53 and ECH. These models were generated with olivine (O) and mafic kimberlite nodule (K) (Mainprice & Silver 1993) elasticity tensors. Angle is the backazimuth and radius is the angle of incidence for 200 km depth out to 30°. Black lines represent the apparent splitting measurements (ASM) as in Fig. 4. Grey lines are the predicted ASM corresponding to the best model found via a grid search. Squares represent unconstrained measurements. The model parameters, 2σ error bars, and $R^\star$ are indicated in the box. For the HS53 olivine model, only the predictions for the specific data are shown because the dt predictions become extremely large on the western side of the quadrant.

that, for a two-layer model, UCONS occur in two locations of periodicity P along the IPA axis, which ranges from 0°–180°. Therefore, to use the UCONS, we simply measure the deviation in IPA from the P zones to the UCONS that are located within ±45° of the P zones. To add this misfit to the error-normalized non-null misfit, we created synthetic split waveforms arising from a two-layer anisotropy model, added noise, filtered the waveforms from 5–50 s, and found that, for typical noise levels, the maximum 2σ deviation in IPA is roughly 20°.

The TL modelling results for both data sets (NUCONS and YUCONS) are presented in Table S2 (available in the online version of the journal). The best models for which $R^* > 0.25$ are also plotted in Fig. 6 (bold stations: BFO, CLZ, HS53, NE38). The most convincing fits occur for stations HS53 ($R^* = 0.57$) and BFO ($R^* = 0.58$). Numerically, the optimum two-layer model we obtain for BFO has upper and lower splitting parameters $\phi_u = 0°$, $dt_u = 1.1$, $\phi_l = 70°$, and $dt_l = 2.3$. However, the 95 per cent confidence region was truncated by the dt_l maximum grid boundary (3.5 s), and so the error bars have not been determined, casting this model into question. This model is very similar to the model determined by Vinnik *et al.* (1994) (parameters $\phi_u = 10°$, $dt_u = 1.1$, $\phi_l = 82°$, and $dt_l = 1.9$) for stations CLZ, BFO, and FUR. Their model was determined by assuming that the same anisotropy existed beneath these stations, then forward modelling the apparent splitting by perturbing an initial model that was consistent with previous ϕ observations via *SKS* splitting (Vinnik *et al.* 1992) and azimuthal variations in P_n velocity (Bamford 1977).

Although the optimum TL model for BFO has $R^* = 0.58$ and is consistent with the model reported by Vinnik *et al.* (1994), the model was only one out of five possible models (out of 62 local minima). When we use the YUCONS data set, we obtain a different model ($\phi_u = 40°$, $dt_u = 1.4$, $\phi_l = 90°$, and $dt_l = 1.2$) with $R^* = 0.52$. This latter YUCONS model is similar to the other four possible NUCONS models. For our optimum TL model, we therefore prefer that provided by the YUCONS data set ($\phi_u = 40°$, $dt_u = 1.4$, $\phi_l = 90°$, and $dt_l = 1.2$), even though the model fit is slightly less good than that provided by the NUCONS data set. We note that $\phi_u = 40°$ is between the P_n fast orientation of Bamford (1977) (20°) and that of Smith & Ekström (1999) (53°) for the west Germany/east France region. In addition, ϕ_u is similar to that for the optimum TL model for HS53.

3.1.6 Comparison between dipping-axis and two-layer models

Splitting at most stations that exhibit complexity can be explained in part by either dipping-axis anisotropy and/or two-layer anisotropy with horizontal fast axes (Fig. 7; Table S2). These models are clearly different, but at some stations fit the data equally well.
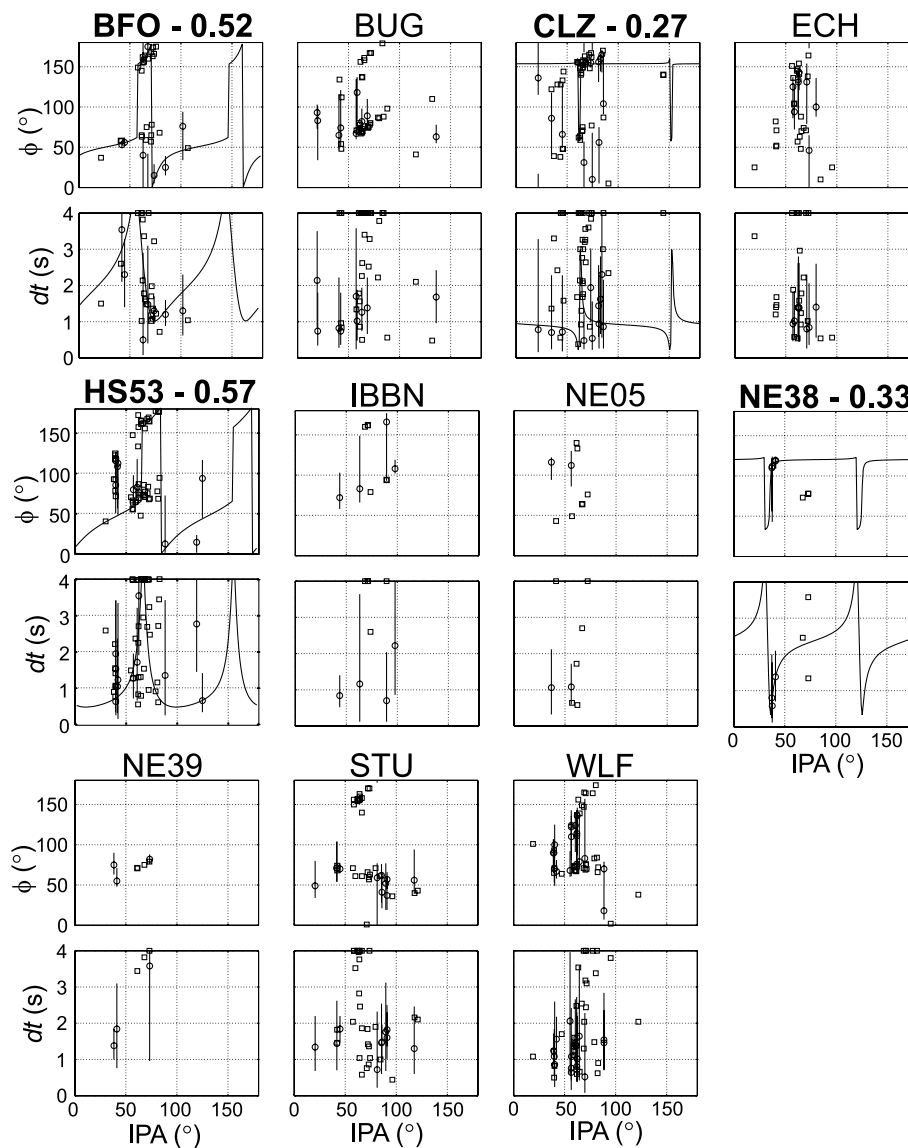
Figure 6. Splitting measurements as a function of initial polarization azimuth. Circles and error bars indicate constrained fast polarization azimuth and delay times. Squares are unconstrained measurements. The predictions for models with $R^\star > 0.25$ are shown, with $R^\star$ indicated next to the station name (bold stations; see also Fig. 7).

The DA models for NE38, CLZ, HS53, WLF and ECH require very large layer thicknesses (520, 810, 1260, 603 and 145 km). Most of these thicknesses are physically unreasonable. Making a simple Fresnel-zone argument assuming 360° of BAZ coverage (Alsina & Snieder 1995; Wylegalla *et al.* 1999; Rümpker & Ryberg 2000), even if minor anisotropy associated with a ~800-km-thick layer exists beneath one of these stations, approximately the same anisotropy and splitting patterns should be observed for stations separated by as much as 350 km. WLF and HS53 are separated by only 200 km, and the optimum TL models for these stations are quite different.

Stations ECH, BFO, and STU effectively form a transect with a ~100-km spacing. The only tectonic structure or characteristic that may not affect the underlying crust/mantle beneath the entire 300-km length in roughly the same fashion is the Rhine graben. However, if the optimum models are to be believed, there is no spatial correlation between optimum models (DA model for ECH, TL model for BFO, and HA model for STU). Laterally varying

anisotropy beneath the Rhine graben as suggested in Fig. 4 could instead explain splitting beneath this transect.

In summary, splitting at the stations that exhibit complexity is roughly modelled just as well with either the TL or DA model— two model types that lead to very different interpretations. More importantly for the DA and even more so for the TL models, between adjacent stations (e.g. ECH, BFO, STU) for each model type there is not the convincing consistency that one might expect given that most current and past tectonic processes in the region probably occurred over scales that are larger than the spacing of the seismic stations. In addition, grid searches for the models produce at least a few possible solutions and many more local minima. These observations suggest that either the DA or the TL model is not the correct model to explain splitting beneath west-central Europe, or that additional anisotropic complexity is perturbing the simple splitting variation that is expected for the true DA or TL model to the extent that the range of IPA, BAZ, and INC included in our data set is not sufficient to resolve the correct model given our data uncertainties.
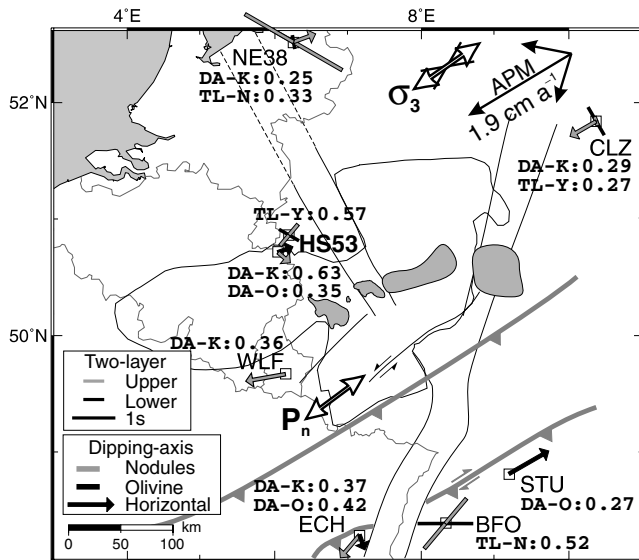
Figure 7. Dipping-axis (DA) and two-layer (TL) anisotropy models for stations with $R^\star > 0.25$. DA models were generated with olivine (O) and mafic kimberlite nodule (K) elasticity tensors. TL modelling used two different data sets: with unconstrained measurements (Y) and without (N). Models for composite station HS53 are separated for display purposes.

We therefore do not accept our DA and TL models in Table S2 as being physically realistic. Rather, we think a smoothly varying single-layer model with a horizontal fast axis explains the first-order anisotropy beneath each station.

3.2 Eifel Network splitting measurements

The Eifel network recorded at most two *SKS* phases of sufficient quality to make splitting measurements (Fig. 2; Table S1, available online) because the region rarely receives high-quality *SKS* phases on account of its location with respect to the dominant earthquake generation zones. The first recorded event (1997 November 28) was a $M_w = 6.7$ from ~585 km depth beneath the Peru–Chile border region. The second event (1998 May 21) was a shallow $M_w = 6.7$ event that occurred near the Minahassa Peninsula, Sulawesi, in the western Pacific. The BAZs of these events are ~180° apart, which offers no capability of resolving TL anisotropy models, but does offer the capability of rejecting them if the measurements are different. The INCs for these *SKS* events are 10°–13°, which are insufficient for resolving most dipping fast-axis models of anisotropy. Because the mobile stations were relocated midway through the experiment, and the events occurred at opposite ends of the deployment, most of the stations only recorded one of these events.

The apparent splitting measurements for the Eifel Network are presented in Table S3. The resulting adequately constrained measurements have average 2σ error bars for ϕ and dt of $\pm 20°$ and ± 0.8 s. The poorly constrained measurements have errors of $\pm 50°$ and ± 1.3 s, but are still clearly not UCONS, as indicated by the shape and size of their confidence regions. There were a handful of stations that displayed a very long dt of between 2 and 3.5 s. These measurements are associated with well-constrained confidence regions, which suggest that they are valid measurements. Although many measurements are constrained, there were also many clear UCONS, which we view as important constraints for splitting beneath the

Eifel, given our lack of additional data. Most UCONS occurred for stations west and southwest of the Eifel volcanic fields.

3.3 Station splitting averages (preferred splitting models)

We use the stacking method of Wolfe & Silver (1998) to calculate station splitting averages when more than one event per station is analysed. This technique works by performing the splitting analysis on a suite of split waveforms, summing the measurement misfit functions, and finding the global minimum (ϕ and dt). This effectively averages out splitting variation, and gives the best model parameters (ϕ and dt) of a single-layer anisotropy model with a horizontal fast axis (HA model). The results from modelling the splitting observed at most nearby permanent stations suggest that this method is a permissible approach to treating the west-central European splitting data.

Our final splitting results are presented in Fig. 1, and Tables S2 and S4. The station average for splitting at CLZ yields a very short dt. This is probably due to the interference of the vastly different apparent splitting measurements from different BAZs and INCs (Fig. 4). Most of the stations in the Netherlands and northwest Germany have ESE-SE ϕ with ~1.0 s dt. To the south, ECH has an ESE ϕ with a short dt. BFO and STU have a longer dt with a NE ϕ. The increase in dt away from the graben, and the large distribution of null measurements for subgraben ray paths, suggests that beneath the Rhine graben there is little if any anisotropy.

There are some very interesting splitting variations observed around the Eifel hotspot. Our most remarkable observation is the ϕ rotation around the Quaternary volcanic fields from northwest Eifel to northeast Eifel to southeast Eifel to southwest Eifel (Figs 1 and 8). The good SNR of the waveforms analysed, the intermediate-to-small splitting model confidence regions, and the gradual nature of the rotation clearly indicate that this variation is not a result of noise.

The dt across the hotspot varies between 0.5 and 3.5 s. There is clear energy observed on the transverse component that is associated with elliptical horizontal particle motion, an unambiguous observation of splitting. Inspection of the misfit grids show no signs of cycle skipping as an explanation for these long dt. The only pattern in the observed dt is that most of the very long dt occur just south of the east and west Eifel volcanic fields, the locations of Quaternary volcanism. If the long dt were simply a result of coherent noise that was not removed by the SNR > 20 data retention threshold, one might expect long dt from a random distribution of stations.

There are a number of UCONS recorded by the Eifel Network, especially to the west and southwest (white crosses; Fig. 1). The BAZs of the two Eifel events are ~180° apart. Because some null stations occur adjacent to stations with constrained measurements that have ϕ subparallel to BAZ, we interpret these UCONS measurements as showing that the fast axis of anisotropy is parallel or perpendicular to the BAZ ($\pm 5°$).

There are also places where rapid lateral variations in ϕ and dt are observed. These stations appear to be more proximal to the volcanic fields. In general, we interpret the variation in dt to be less significant than that in ϕ because measurements for cases where $\phi \approx$ IPA yield a greater degree of uncertainty in dt than in ϕ. The very long dt are associated with ϕ that are roughly parallel to the IPA (Fig. 1). While this may suggest that these measurements are invalid, the fact that they are consistent between nearby stations in some places, and, to a lesser extent, that similar ϕ farther from the volcanic fields have much shorter dt, suggests that these results are valid. The variation in ϕ, though, is better constrained, and there are clear examples where there are rapid variations in ϕ over short distances.
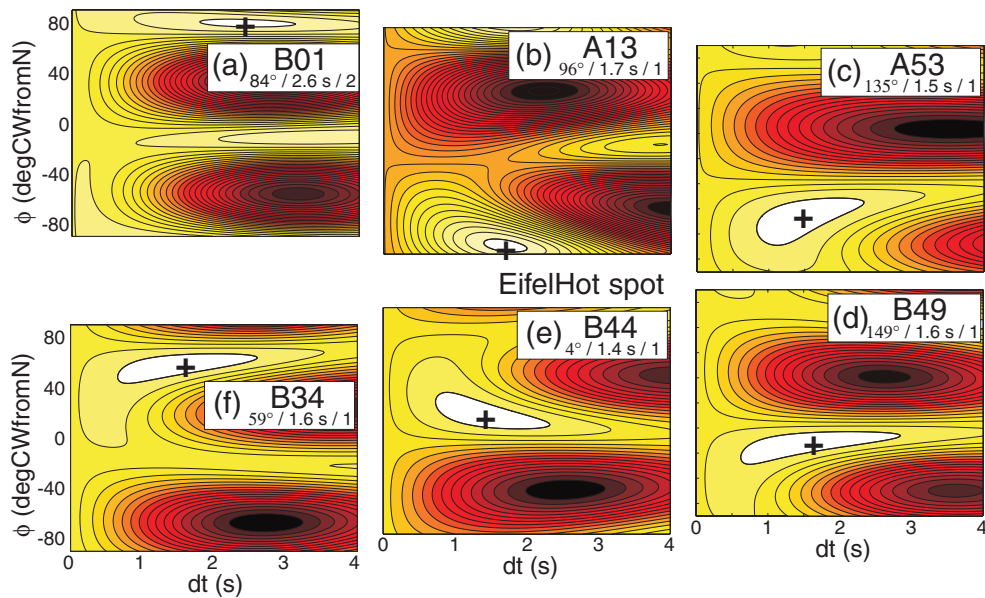
Figure 8. Examples of station splitting across the Eifel Network (a–f). The optimum splitting parameters (global misfit minima) are shown by the crosses, and the 95 per cent confidence regions are indicated in white. The white box gives the station name, splitting estimate (ϕ and dt), and number of events analyzed. A clockwise rotation of the fast direction (ϕ) is observed around the Eifel volanic fields (a–f; see Fig. 1 for locations).

4 ANISOTROPY INTERPRETATION

The ϕ rotation around the east Eifel volcanic field is a first-order feature obviously not predicted by a uniform fast-direction model such as the fossilized lithospheric anisotropy model that predicts ϕ throughout most of Europe to be parallel to the ENE Hercynian basement structural trends (Silver 1996). The values of dt that we observe across the Eifel hotspot vary between extremes. However, based on our experience with splitting on the regional permanent stations, we expect that dt averages of many additional data would show considerably less variation and that these dt averages would not systematically decrease with thinning of the lithosphere towards the Eifel region.

An alignment of magma-filled lenses leads to a bulk anisotropy with ϕ parallel to the strike of the lenses. Kendall (1994) showed that, for ~10 per cent partial melt in the lithosphere/asthenosphere, dt could be as long as 2–3 s. With different melt porosities, degrees of alignment, lens geometries/densities, or melt-zone thicknesses, dt could be even longer (Walker *et al.* 2004a). Recent receiver-function results have found evidence for 1 per cent melt beneath the Eifel (Budweg 2003). Lateral variations in melt porosity and degree of lens alignment in the lithosphere/asthenosphere might explain the magnitude and variation of dt across the Eifel. However, this model requires the lenses to be vertical, and the stress in the zone of partial melt to be in a normal-faulting stress state with a direction that varies greatly over short lateral distances. We expect the direction to change smoothly over 100–1000 km, as it does in the near surface of west-central Europe (Mueller *et al.* 1997), and therefore believe that the variation in ϕ is not easily explained by a model of magma-filled lenses.

Extension of the lithospheric mantle could lead to the development of a lattice preferred orientation (LPO) of olivine fast a-axes. Extension has been in the ENE orientation in the Eifel region, perpendicular to the opening of the Rhine graben (Mueller *et al.* 1997). Splitting analyses in the East African Rift system in Kenya and Tanzania show that lithospheric extension there does not lead to

a significant development of olivine LPO (Walker *et al.* 2004b). We note that there are rift-perpendicular ϕ across the Rur graben, around the east Eifel volcanic field and at station NE39 (Fig. 1). However, these ϕ are no different from some others observed elsewhere around the hotspot that are not near the graben, and this model does not explain splitting variation elsewhere, especially the NW ϕ NE of the Rur graben. Furthermore, this mechanism does not work in the southern Rhine graben near stations ECH and BFO, where subgraben ray paths did not detect resolvable rift-perpendicular splitting.

We think that the most probable explanation of splitting beneath the Eifel is that it is predominantly asthenospheric in origin (explaining the long dt in some places), but perturbed by additional lithospheric and/or asthenospheric anisotropy (explaining the rapid lateral changes in some places). Because evidence exists for a mantle upwelling beneath the Eifel hotspot (e.g. Ritter *et al.* 2001; Keyser *et al.* 2002), we search for an upwelling model that satisfactorily predicts the general pattern of observed ϕ.

4.1 Parabolic asthenospheric flow (PAF) modelling

Using a finite-difference approach incorporating temperature, pressure, and rheology, Ribe & Christensen (1994, 1999) and Moore *et al.* (1998) modelled the steady-state 3-D interaction between the moving Pacific plate and the hypothesized Hawaiian plume. The asthenospheric flow patterns in their models are intuitive, with subvertical flow near the conduit, corner flow where the conduit encounters the plate, and subhorizontal flow elsewhere. In map view, the flow patterns are approximately parabolic in shape, and develop in response to the gravitational spreading of the buoyant upwelling material and the drag associated with plate motion. Kinematically similar solutions of parabolic asthenospheric flow (PAF) have been obtained analytically (Sleep 1987; Richards *et al.* 1988) and with lubrication theory (Olson 1990). We test for a PAF model beneath the Eifel hotspot using such a kinematic approach (see Supplementary Material available online for details).
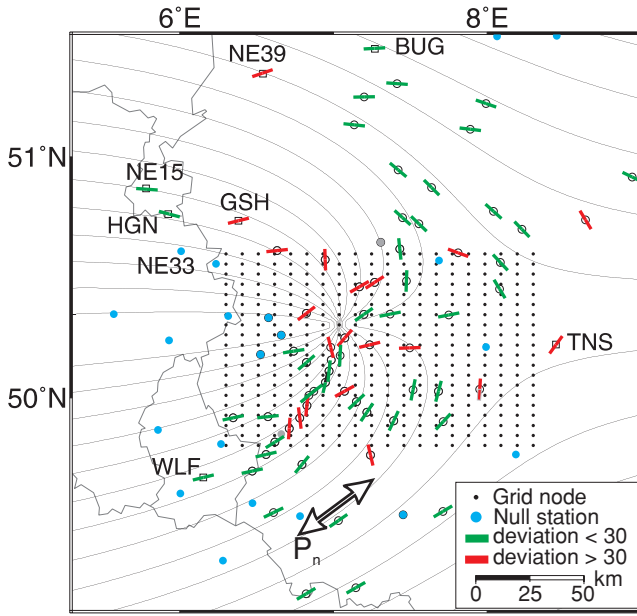
Figure 9. Testing the optimum PAF model predictions for the Eifel hotspot. Lines: station fast polarization azimuths (ϕ). Grey circles: stations that only recorded unconstrained measurements. Black curves: asthenospheric horizontal flow lines of the optimum PAF model. The spatial variation of the flow predicts 61 per cent of the spatial variation in ϕ, suggesting that there is an upwelling conduit beneath the Eifel hotspot.

To test the PAF-model predictions of ϕ, we first select a subset of the data spanning a 270×270 km area surrounding the Eifel hotspot, the area most likely to experience the greatest hotspot-related geodynamic effects (Fig. 9). We then perform a grid search, over the four model parameters: upwelling conduit latitude/longitude, parabolic width (also known as the stagnation distance; Sleep 1990), and the absolute plate motion. The 2-D streaming potential function (Milne-Thomson 1968) for the PAF model is given by

$$\psi = \frac{y}{P} + \tan^{-1}\left(\frac{y}{x}\right), \tag{2}$$

where P is the parabolic width (km), and x/y are the spatial coordinates. The upwelling centre is at the origin, and the function is symmetric about the x-axis. The pattern is horizontally rotated to the azimuth that corresponds to the APM direction, then translated to the trial upwelling centre location. The final PAF flow lines and predicted fast azimuths are given by the contours of this function, or the orientation perpendicular to the gradient of ψ:

$$\phi^* = \frac{d\psi}{dy}\hat{x} + \frac{d\psi}{dx}\hat{y}, \tag{3}$$

where ϕ^* is the predicted fast orientation. We minimize the difference between ϕ^* and the observed fast azimuths with an L2 misfit function:

$$M_{PAF} = \sum_{i=1}^{n} \left(\phi_i^* - \phi_i\right)^2, \tag{4}$$

where $n = 67$ is the number of constrained fast azimuths.

We estimate the optimum model and standard deviation with a bootstrap method (Efron & Tibshirani 1998). The bootstrap method uses a master data set comprising the constrained station fast azimuths, and creating B different data sets of length n by sampling the master data set with replacement. For each data set, the grid search is employed, and an optimum model vector α is determined

by the global misfit minimum. The bootstrap technique is an unbiased estimator of the mean and standard error. The bootstrap mean is simply the mean of the optimum models, and the bootstrap error for the ith model parameter α_i is

$$\sigma_i = \sqrt{\sum_{b=1}^{B} \frac{[\alpha_{i,b} - \bar{\alpha}_i]^2}{B-1}}, \tag{5}$$

where $\bar{\alpha}_i$ is the mean of the B optimum α_i model parameters. Practical values of B range from 50–200 (Efron & Tibshirani 1998), and we use $B=100$. We find that the best-fitting PAF pattern is centred at 50.31°N, 7.04°E, has a parabolic width of 60 km, and opens towards 262°. This model explains 61 per cent of the variation in the data. Additional techniques generally produce similar optimum models and uncertainties (Walker 2004). Most of the flow lines are within $\pm 30°$ of the observed ϕ (Fig. 9).

To explore trade-offs in the modelling parameters and the degree of non-uniqueness, we inspect the marginal misfit curves, 2-D projections of the local and global minima, and 1-D histogram projections of the misfit space (Fig. 10). Although there are many local minima, the global minimum is the only minimum that falls below the critical misfit threshold corresponding to the 95 per cent confidence contour, clearly indicating a robust result. We also find that the optimum model is not significantly different when we include the UCONS in our modelling.

We perform an F-test for nested models to determine if the improvement of fit for the more complicated PAF model is significant given the increase in the number of modelling parameters (Mendenhall & Sincich 1995). The F ratio is

$$F = \frac{(M_o - M_{PAF})/M_{PAF}}{(DF_o - DF_{PAF})/DF_{PAF}}, \tag{6}$$

where M_o and M_{PAF} are the sum-of-square misfits for the single-azimuth model and PAF model, and the DFs are the associated total degrees of freedom. If the simpler model is correct, one would expect the relative decrease in the sum-of-squares to be approximately equal to the relative decrease in the total degrees of freedom ($F \approx 1.0$). If the more complicated model is correct, then one would expect the relative decrease in the sum-of-squares to be greater than the relative decrease in the total degrees of freedom ($F \gg 1$). The various misfits and degrees of freedom are $M_o = 13 \times 10^4$, $DF_o = 66$, $M_{PAF} = 5 \times 10^4$, and $DF_{PAF} = 63$, which leads to $F = 34$. The p-value is the probability that our splitting data set could have been observed given the assumption that the single-azimuth model is correct. The p-value for $F = 5.0$ given the degrees of freedom for the PAF model is 0.0015 (a 0.15 per cent chance). The p-value for our calculated $F = 34$ is effectively 0. Hence, we can reject the single-azimuth null hypothesis in favour of our more complicated PAF model.

5 DISCUSSION

The Eifel PAF model predicts 61 per cent of the ϕ variation from a single-azimuth model (Figs 9 and 10). The Eifel stations that show rapid splitting variations could be considered as outliers, and part of the source of the 39 per cent misfit. These stations typically only recorded one event. While we consequently do not consider the rapid lateral variations in splitting across the Eifel to be of crucial importance, we recognize that they may still be tectonically significant and may suggest the existence of lateral and possibly vertical variations in a layer of anisotropy that may exist, in part, at shallow depths.

The lithosphere beneath the Eifel region is ~50–70 km thick (Panza *et al.* 1980; Babuška & Plomerová 1993; Glahn & Granet
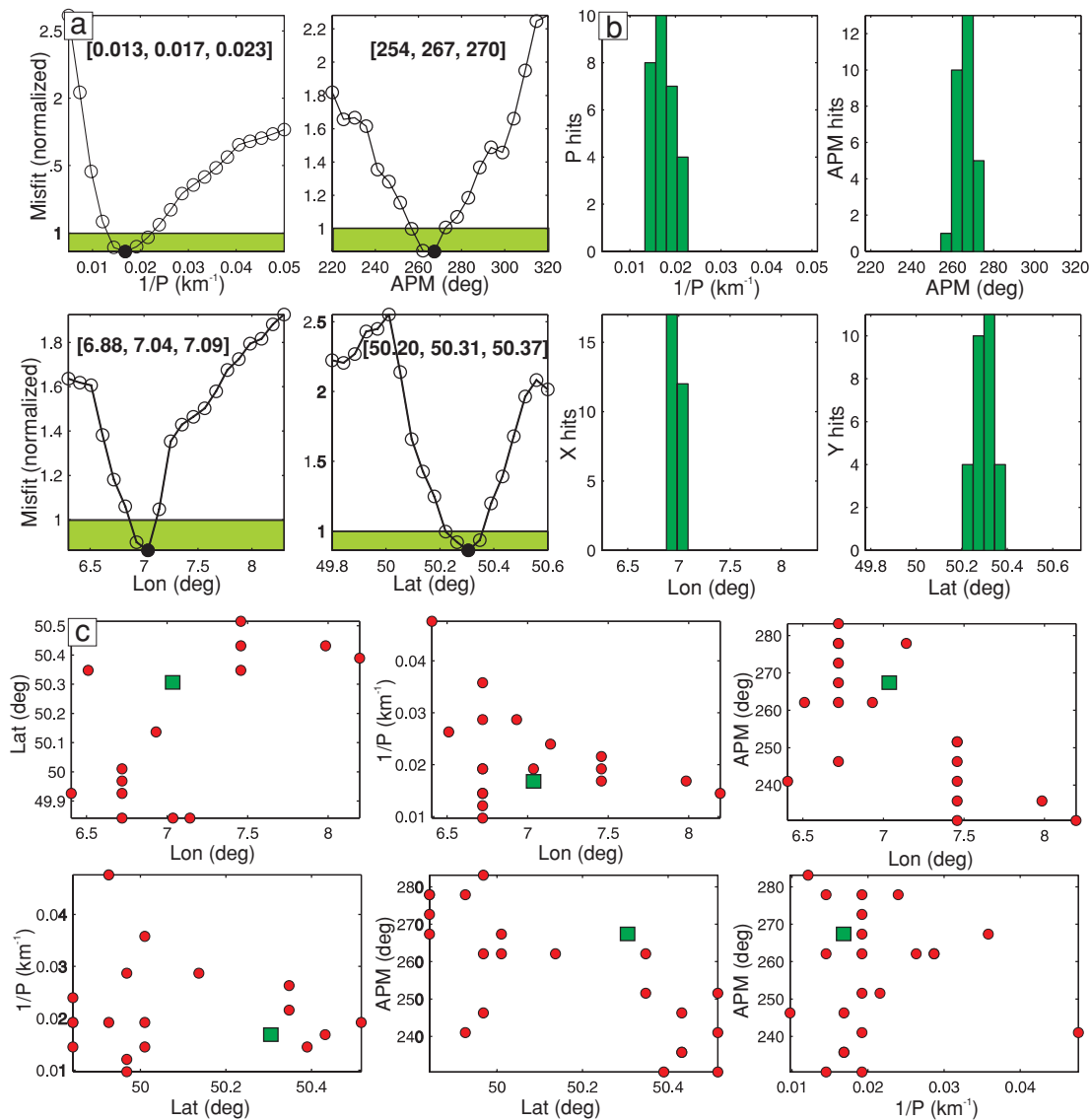
Figure 10. Confidence tests of the optimum parabolic asthenospheric flow (PAF) model. The model parameters are the latitude/longitude of the plume centre, the parabolic width (P), and the absolute plate motion direction (APM). (a) The marginal misfit curves, where the solid circle represents the optimum model, the horizontal line is the 95 per cent confidence level, and the optimum parameters and 95 per cent confidence region are indicated in brackets. (b) Histograms of the results of randomly targetting nodes in the misfit grid and testing if they are below the 95 per cent confidence contour. (c) 2-D projections of the locations of local minima, where the squares indicate the optimum solution, and the solid circles represent local minima that are not possible solutions.

1992; Glahn *et al.* 1993). The depth at which overlap becomes significant for *SKS* Fresnel zones at two adjacent stations is not clearly defined (Alsina & Snieder 1995; Wylegalla *et al.* 1999), but Rümpker & Ryberg (2000) found that, for an abrupt lateral change in the parameters of an anisotropic layer at a depth of 100–250 km for a signal period of 8 s, the variation in ϕ/dt that occurs over 30 km could be at least $30°/1.0$ s. However, only some of the lateral variations we observe can be explained by such a model. The other lateral variations could be explained better by stronger contrasts in anisotropy and/or anisotropy at shallower depths (Rümpker & Ryberg 2000). The upper layer of anisotropy in a medium of slowly varying anisotropy (Rümpker & Silver 1998) or two-layer anisotropy (Saltzer *et al.* 2000) has the strongest effect on the final station splitting estimates. Fossilized lithospheric anisotropy is supported by the existence of LPO fabrics in mantle xenoliths from the west Eifel region. These tabular recrystallized spinel peridotites show the or-

thorhombic 'Dreiser Weiher' fabric (e.g. Mercier & Nicolas 1975), and come from a shallow mantle depth (*ca.* 40 km). The 1 per cent partial melt beneath the Eifel could also be a source of additional anisotropy (Budweg 2003). Finally, an additional mechanism that may explain the observed splitting variation is the effect of dynamic recrystallization during LPO generation in the region of corner flow near the conduit. Kaminski & Ribe (2002) show that LPO fast directions may not be locally parallel to the flow lines in the proximity of the conduit, but are parallel at greater distances from the conduit. The effect on *SKS* splitting, which is an integrated measure of anisotropy along the ray path, has not yet been determined, but is likely to be complicated and to lead to lateral variations for individual splitting measurements. The long *dt* observed at several stations near the hotspot (Fig. 1) may also be consistent with the Kaminski & Ribe (2002) results, which predict strong anisotropy where the fast orientation is aligned parallel to the flow direction
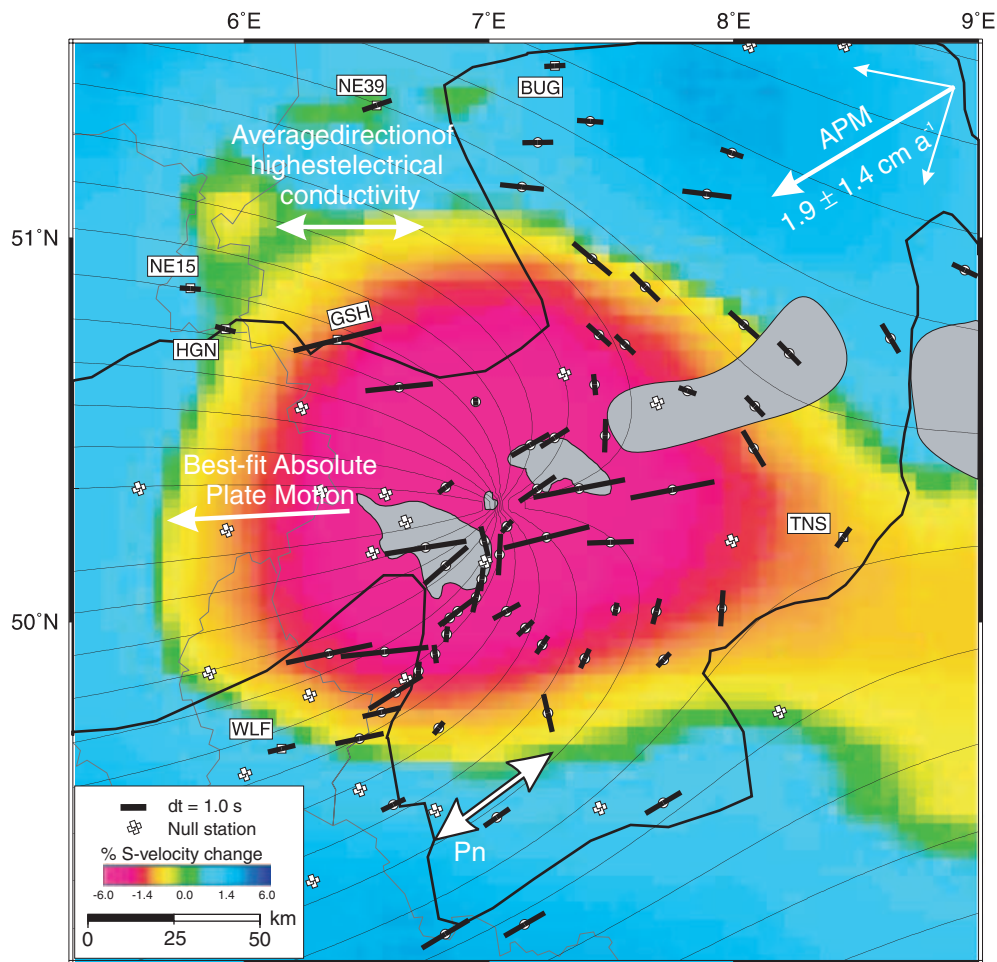
Figure 11. Station splitting estimates, optimum parabolic asthenospheric flow model, and shear-wave velocity anomaly (30–100 km depth; Keyser *et al.* 2002). Note the good correlation between the locations of the best-fitting upwelling centre, the Quaternary volcanic fields, and the 5 per cent slow velocity anomaly. Note also the location of the long delay times. The best-fitting absolute plate motion is approximately towards the west, is subparallel to the average direction of highest electrical conductivity in the asthenosphere (Leibecker *et al.* 2002), and is within the 95 per cent confidence region of the HS3-NOVEL 1A absolute plate-motion direction (Gripp & Gordon 2002).

slightly downwind of the conduit. We therefore suggest that the 39 per cent variation not fit by the PAF model may be due to un-modelled signal from local domains of fossilized anisotropy, concentrations of aligned magma lenses or partially molten dykes in the lithosphere, and/or the effects of dynamic recrystallization associated with corner flow near the conduit.

The optimum PAF model is consistent with other data (Fig. 11). The most obvious consistency is that the predicted upwelling conduit is located at the centre of the *S*-wave velocity anomaly between 30 and 100 km depth (Keyser *et al.* 2002). This location is between the east and west Eifel volcanic fields, the youngest (Quaternary) volcanic centres associated with the Rhenish Massif. HS3-NUVEL1A is a recent global absolute plate motion model that uses newly refined volcanic trends and propagation rates to calculate plate velocities, resulting in a 3-D error ellipsoid volume that is about half that of the ellipsoid used in the HS2-NUVEL1 model (Gripp & Gordon 1990, 2002). The optimum plate motion direction from our PAF model is $262° \pm 23°$ (out of a possible $360°$), which is within the 95 per cent uncertainty of the refined Eurasian plate motion ($239° \pm 44°$). Our predicted plate motion direction also approximately correlates with the eastward average orientation of maximum electrical con-

ductivity (Leibecker *et al.* 2002) E in the asthenosphere across the Rhenish Massif. Leibecker *et al.* (2002) show that this anisotropy could be due to an LPO of olivine fast a-axes in the asthenosphere, with the electrical conductivity amplified by the presence of water, which allows much more efficient charge transfer via the diffusion of hydrogen along the crystallographic olivine a-axes.

Bormann *et al.* (1993) and Silver (1996) suggested that variations in splitting fast directions across Europe that are not predicted by simple plate drag for a flat lithosphere/asthenosphere boundary could be explained by fossilized anisotropy in the lithosphere associated with lithospheric structures inherited during the Hercynian orogeny. Many ϕ throughout our study area are not parallel to the Hercynian structures, yet *dt* is comparable with values in central and eastern Europe. Bormann *et al.* (1996) suggested that the changes in lithospheric thickness across Europe could give rise to edge flow parallel to the contours of the basal lithospheric topography, for a plate moving through a resistive asthenosphere. They find a good correlation between most ϕ and the orientation of Moho contours, which they claim are a proxy for the lithospheric thickness contours. Our interpretation of asthenospheric anisotropy as the dominant splitting source in west-central Europe is consistent with that

of Bormann *et al.* (1996). A comparison of accurate lithospheric thickness variations with existing published station splitting estimates (and other observations of anisotropy) is necessary to better distinguish the origin of anisotropy beneath Europe.

A PAF model is consistent with splitting beneath the Great Basin (Savage & Sheehan 2000; Walker *et al.* 2004a) and the Hawaii hotspot (Walker *et al.* 2001, 2003; Vinnik *et al.* 2003). However, such a model does not predict the observed splitting around the Afar (Ayele *et al.* 2003; Gashawbeza *et al.* 2004), Iceland (Bjarnason *et al.* 2002), and Massif Central (Barruol & Granet 2002; Barruol *et al.* 2004) hotspots. It is unlikely to be a coincidence that a PAF pattern is consistent with splitting around the Eifel (variance reduction of 61 per cent), Great Basin (variance reduction of 64 per cent; Walker *et al.* 2005), and Hawaii hotspots. Rather, the success of these models in explaining most of the splitting variation implies that plume-like upwellings can lead to a predictable pattern of anisotropy and can therefore be one diagnostic in testing between upwellings and alternative models for mantle hotspots (Walker *et al.* in press).

The Eifel hotspot has a volcanic, topographic, *P*-velocity (Ritter *et al.* 2001), *S*-velocity (Keyser *et al.* 2002), *Q* (Meyer 2001), receiver-function (Grunewald *et al.* 2001), geochemical (Wilson & Patterson 2001), and mantle-anisotropy anomaly that suggest a weak plume-like upwelling with a low excess temperature and volumetric flow rate. Receiver functions across the Eifel (Grunewald *et al.* 2001) suggest anomalously hot material in the vicinity of the 410-km discontinuity, but none near the 660-km discontinuity. Montelli *et al.* (2004) found beneath the Eifel a low-velocity anomaly in the upper mantle, but not in the lower mantle. We suggest that the source of the upwelling is a fluctuating temperature perturbation along a boundary layer in the mantle transition zone.

Theoretical models have suggested that *SKS* splitting should not occur in an upwelling conduit since the flow in the conduit is vertical, which would predict, under simple assumptions, vertical fast a-axes in and along the side of the conduit (e.g. Rümpker & Silver 2000). The relationships between olivine water fugacity and LPO anisotropy (Karato 2003) suggest that high water fugacity selectively enhances the mobility of b=[001] dislocations more than that of the b=[100] dislocations. For a vertically flowing asthenosphere of high water fugacity, one may find an alignment of intermediate olivine c-axes in the vertical direction, and possibly olivine fast- and/or slow-axes in the horizontal plane, suggesting that splitting observed above a hotspot could be a result of LPO anisotropy in a wet upwelling. Beneath the Eifel hotspot, however, Keyser *et al.* (2002) suggest that a dehydration process is occurring between 170 and 240 km depth, preferentially removing water with upward migrating melts. Therefore, if high water fugacity exists beneath the Eifel, it probably exists at depths deeper than ∼250 km. If the dominant source of anisotropy occurs at those depths, one would observe much less variation in splitting between adjacent stations. Therefore, the seismic observations suggest that, above the Eifel hotspot, the dominant source of splitting is due to horizontal LPO either in the lithosphere and/or just beneath the base of the lithosphere, but they neither suggest nor rule out LPO at deeper levels in and around the conduit.

We can test our PAF model to determine if it is consistent with the 19 ± 14 km Ma^{-1} HS3-NUVEL1A plate-motion speed for the Eurasian plate (Gripp & Gordon 2002; see Supplementary Material). We do not know the rate of the Eifel upwelling, but we do know the parabolic width that explains splitting fast azimuths around Hawaii (∼300 km) (Ribe & Christensen 1994; Walker *et al.* 2001), and the Pacific plate speed (103 ± 9 km Ma^{-1}) (Gripp & Gordon 2002).

The PAF model is a 2-D approximation to the 3-D problem. Using conservation of mass, we can extend this 2-D approximation into the depth dimension if we introduce the thickness of the mechanical asthenosphere into which the upwelling material spreads. If we use the PAF and other parameters for the Hawaiian upwelling (Ribe & Christensen 1999) and the Pacific plate speed, we can assume that the asthenospheric thicknesses beneath Hawaii and the Eifel are equal, and use Eifel parameters determined from tomographic data (excess temperature/radius of 125 K/55 km) (Ritter 2005), and parameters for olivine deforming via dislocation creep (Karato & Wu 1993) to calculate a viscosity of 3.9×10^{20} Pa s and a maximum buoyancy flow rate of ∼40 kg s^{-1} for the Eifel upwelling, which are roughly similar to those calculated by Ritter (2005). We then can use the Hawaiian parameters and equal asthenospheric thickness assumption to calculate a Eurasian plate speed of 12 km Ma^{-1}, which is within the 95 per cent confidence region of the 19 ± 14 km Ma^{-1} HS3-NUVEL1A speed. Although the error bars for this calculation are large due to the inherent uncertainties in the mantle rheology and Eifel upwelling parameters, our PAF model determined from splitting fast azimuths is consistent with a slow Eurasian plate motion.

Although our PAF model explains the majority of our splitting data, and is consistent with many other geological and geophysical data, there are issues that need to be addressed if a fixed upwelling exists beneath the Eifel hotspot, the most obvious being the lack of an observed hotspot track with an age progression, which would be expected for a moving plate. The Rhenish Massif volcanic centres form a roughly ENE lineation (Fig. 11), but there is no consistent age progression. If the current plate speed (19 km Ma^{-1}) has been consistent since the onset of volcanism at the eastern end, there should be a ∼500-km long hotspot track. The entire lineation is only ∼250 km long. All the data that suggest that an upwelling exists beneath the Eifel can only be consistent with the lack of an age progression if (1) the upwelling is weak and generates sporadic eruptions, possibly dependent on changes in lithospheric stress and/or the arrival of new hot material to the base of the plate, and (2) either the Eurasian plate speed has varied considerably over the last 28 Ma or the Eifel upwelling flow is complex and periodic upwellings do not follow a common path.

Tomographic inversions around hotspots typically ignore the effect of anisotropy because it is presumed to be weak (∼1–5 per cent), as suggested by mantle xenoliths (Mainprice & Silver 1993). Keyser *et al.* (2002) looked at relative traveltimes across the Eifel Network for 61 direct *S* and 17 *SKS* events on the radial and transverse components, and searched for consistent differences in traveltime between the radial and transverse first arrivals. They report no first-order delays, which to them suggests that anisotropy has not significantly affected their tomographic images. However, the integrated effect of anisotropy on teleseismic waves causes peak-to-peak split shear-wave delay-time variations of typically 0.5–1.5 s, and, in our Eifel case, of 0.5–3.5 s. This suggests that the observed peak-to-peak 4–6 s *S*-wave relative delays observed by Keyser *et al.* (2002) may be affected by the anisotropy beneath the network for some of the stations. It still remains to be determined if (1) the traveltime residual not predicted by their most basic *S*-wave tomographic image can be explained by the seismic anisotropy that we observe, or (2) the tomographic inversion, after correcting for the effects of anisotropy as observed by shear-wave splitting, would resolve the same upwelling structure. We point out that we used a different data set from that used by Keyser *et al.* (2002). We applied a bandpass filter between 5 and 50 s to obtain two *SKS* waveforms that provided constrained splitting measurements with energy SNR > 20. Keyser *et al.* (2002)

analysed 17 *SKS* events using a 1–14 s bandpass filter, and obtained an average energy SNR of 10. It might be that the reason the centre of the slow velocity anomalies associated with the Eifel hotspot varies by 60–120 km between *P*-wave, *S*-wave, and surface-wave studies is a result of not correcting for the effects of anisotropy that we observe in shear-wave splitting.

Babuška & Plomerová (1992) analysed the directional dependence of *P*-wave residuals and found evidence of northwest-dipping fast *P* orientations in the Rhenohercynian and Saxothuringian terranes, and southeast-dipping fast orientations in the Moldanubian terrane. Our optimum dipping-axis models are not consistent with their results. We note that it is difficult to isolate the effects of velocity heterogeneity from those of upper-mantle anisotropy on teleseismic waveforms. Given this difficulty, and the fact that our modelling results for more complicated anisotropy models are ambiguous, this inconsistency is not surprising.

6 CONCLUSIONS

Our shear-wave splitting results suggest that the anisotropy beneath the Eifel hotspot and surrounding Rhenish Massif is mostly contained in the asthenosphere. In general, the data from the permanent stations cannot be fit satisfactorily with a simple, unique two-layer or dipping-axis anisotropy model. The splitting variations observed around the southern Rhine graben may be explained by lateral variations in anisotropy, with different fast directions on either side of the Rhine and little-to-no azimuthal anisotropy beneath the Rhine. The best fit at most of the other stations is provided by a single-layer model with a horizontal fast axis, the regional average of which is oriented ENE–WSW.

The observed fast polarization azimuth (ϕ) and delay time (dt) change remarkably across the Eifel hotspot. The longer dt and variation of ϕ cannot be explained by a fossilized unidirectional LPO anisotropy in the lithosphere. The least horizontal compressive stress is not parallel to ϕ across the Rhenish Massif, which would be expected if ENE–WSW lithospheric extension was generating an LPO of olivine in the lithosphere. The lack of a correlation between ϕ and the maximum horizontal compressive stress in the upper crust is not consistent with the magma-filled lenses interpretation for the dominant source of splitting.

Our preferred interpretation is that the splitting is due to parabolic asthenospheric flow (PAF), which induces an LPO of olivine in the asthenosphere as a result of simple-shear interaction between a plume-like upwelling beneath the Eifel volcanic fields and the slowly moving Eurasian plate. Specifically, the upwelling material is being fed into a horizontal stream at the base of the Eurasian plate, which is moving towards the WSW relative to a fixed lower mantle. Our PAF model predicts the majority of the ϕ variation. We interpret the remaining unmodelled variation as due to lateral and/or vertical variations in anisotropy associated with fossilized LPO anisotropy in the lithosphere, a shape-preferred orientation of magma-filled lenses in isolated domains of partial melt, and/or LPO anisotropy in the asthenosphere due to dynamic recrystallization associated with lithosphere/upwelling interaction. Our PAF model is generally consistent with recent *P*-, *S*-, and *Q*-tomographic results that image a plume-like structure down to at least 400 km depth, receiver-function results that image a downward deflection of the 410-km phase discontinuity, suggesting anomalously hot mantle material in the upper transition zone, the WSW direction of Eurasian absolute plate motion from global-circuit calculations, and electrical con-

ductivity anisotropy across the Rhenish Massif. The PAF pattern we observe does not suggest anisotropy in the conduit associated with a wet Eifel upwelling.

The ∼300-m Rhenish Massif topographic swell and the tomographic anomalies suggest that the Eifel upwelling is quite slow, and has a low excess temperature, which explains the absence of major volcanism associated with the hotspot. We use our optimum PAF model parameters to calculate a slow Eurasian absolute plate speed of 12 km Ma^{-1}, which is consistent with the recent HS3-NUVEL1A speed. In order to reconcile the evidence that suggests a plume-like upwelling origin for the Eifel hotspot, the lack of an age progression of volcanism, and different published estimates of plate-motion speed for different time periods, we suggest that the Eifel upwelling is sporadic, a result of a low excess upwelling temperature and/or varying crustal stresses that periodically relax and allow eruptions to occur, and speculate either that the currently WSW-moving Eurasian plate direction changed at least once between 6 and 28 Ma, or that the Eifel upwelling flow is complex and the periodic Eifel upwellings do not follow a common vertical path.

REFERENCES

Alsina, D. & Snieder, R., 1995. Small-scale sublithospheric continental margin deformation: constraints from SKS splitting observations, *Geophys. J. Int.,* **123,** 4313–4448.

Ayele, A., Stuart, G. & Kendall, J.-M., 2003. Insights into rifting from shear wave splitting and receiver functions: an example from Ethiopia, *Geophys. J. Int.,* **160,** 342–362, doi:10.1111/j.1365–246X.2004.02206.x.

Babuška, V. & Plomerová, J., 1992. The lithosphere in central Europe—seismological and petrological aspects, *Tectonophysics,* **207,** 141–163.

Babuška, V. & Plomerová, J., 1993. Lithospheric thickness and velocity anisotropy—seismological and geothermal aspects, *Tectonophysics,* **225,** 79–89.

Babuška, V.J., Plomerová, J. & Sileny, J., 1984. Large-scale oriented structures in the subcrustal lithosphere of central Europe, *Ann. Geophys.,* **2,** 649–662.

Babuška, V.J., Plomerová, J. & Sileny, J., 1993. Models of seismic anisotropy in the deep continental lithosphere, *Phys. Earth planet. Inter.,* **78,** 167–191.

Bamford, D., 1977. Pn velocity anisotropy in a continental upper mantle, *Geophys. J. R. astr. Soc.,* **49,** 29–48.

Barruol, G. & Granet, M., 2002. A Tertiary asthenospheric flow beneath the southern French Massif Central indicated by upper mantle seismic anisotropy and related to the west Mediterranean extension, *Earth planet. Sci. Lett.,* **202,** 31–47.

Barruol, G., Deschamps, A. & Coutant, O., 2004, Mapping upper mantle anisotropy beneath SE France by SKS splitting indicates a Neogene asthenospheric flow induced by the Apenninic slab rollback and deflected by the deep Alpine roots, *Tectonophysics,* **394,** 125–138.

Bjarnason, I.T., Silver, P.G., Rümpker, G. & Solomon, S.C., 2002. Shear wave splitting across the Iceland hot spot: Results from the ICEMELT experiment, *J. geophys. Res.,* **107**(B12), 2382, doi:10.1029/2001JB000916.

Bormann, P., Burghardt, P.-T., Makeyeva, L.I. & Vinnik, L.P., 1993. Teleseismic shear-wave splitting and deformations in Central Europe, *Phys. Earth planet. Inter.* **78,** 157–166.

Bormann, P., Grünthal, G., Kind, R. & Montag, H., 1996. Upper mantle anisotropy beneath central Europe from SKS wave splitting: Effects of absolute plate motion and lithosphere-asthenosphere boundary topography?, *J. Geodyn.,* **22,** 11–32.

Brechner, S., Klinge, K., Krüger, F. & Plenefisch, T., 1998. Backazimuthal variations of splitting parameters of teleseismic SKS phases observed at the broadband stations in Germany, *Pure appl. Geophys.,* **151,** 305–331.

Budweg, M., 2003, The upper mantle in the region of the Eifel analysed with the receiver function method, *PhD thesis*, University of Potsdam, Germany.

Campbell, J., Kümpel, H.-J., Fabian, M., Fischer, D., Görres, B., Keysers, Ch.J. & Lehmann, K., 2002. Recent movement pattern of the Lower Rhine Embayment from tilt, gravity and GPS data, *Netherlands J. Geosci.,* **81,** 223–230.

Christensen, N.I., 1966. Shear wave velocities in metamorphic rocks at pressures to 10 kilobars, *J. geophys. Res.,* **71,** 3549–3556.

Crampin, S., 1991. Wave propagation through fluid-filled inclusions of various shapes: interpretation of extensive-dilatancy anisotropy, *Geophys. J. Int.,* **104,** 611–623.

Doebl, F. & Teichmüller, R., 1979. Zur Geologie und heutigen Geothermik im mittleren Oberrhein-Graben, *Fortschr. Geol. Rheinld. Westf.,* **27,** 1–17.

Edel, J.B. & Fluck, P., 1989. The upper Rhenish shield basement (Vosges, upper Rhinegraben and Schwarzwald): Main structural features deduced from magnetic, gravimetric, and geological data, *Tectonophysics,* **169,** 303–316.

Efron, B. & Tibshirani, R.J., 1998. *An Introduction to the Bootstrap, Monographs on Statistics and Applied Probability,* Vol. 57, Chapmann and Hall, New York.

Enderle, U.J., Mechie, J., Sobolev, S. & Fuchs, K., 1996. Seismic anisotropy within the uppermost mantle of southern Germany, *Geophys. J. Int.,* **125,** 747–767.

Farra, V., Vinnik, L., Romanowicz, B., Kosarev, G.L. & Kind, R., 1991. Inversion of teleseismic S particle motion for azimuthal anisotropy in the mantle: A feasibility study, *Geophys. J. Int.,* **106,** 421–431.

Franke, W., 1989. Tectonostratigraphic units in the Variscan Belt of Central Europe, in *Terranes in the Circum-Atlantic Paleozoic Orogens,* Vol. 230, pp. 67–90, ed. Dallmeyer, R.D., Geological Society of America Special Paper, Boulder, CO.

Fuchs, K., 1977. Seismic anisotropy of the subcrustal lithosphere as evidence for dynamical processes in the upper mantle, *Geophys. J. R. astr. Soc.,* **49,** 167–179.

Gashawbeza, E., Klemperer, S., Nyblade, A., Walker, K.T. & Keranen, K.T., 2004. Shear-wave splitting in Ethiopia: Precambrian mantle anisotropy locally modified by Neogene rifting, *Geophys. Res. Lett.,* **31,** L18 602, doi:10.1029/2004GL020471.

Glahn, A. & Granet, M., 1992. 3-D structure of the lithosphere beneath the southern Rhine Graben area, *Tectonophysics,* **208,** 149–158.

Glahn, A., Granet, M. & the Rhine Graben Teleseismic Group, 1993. Southern Rhine Graben: Small-wavelength tomographic study and implications for the dynamic evolution of the graben, *Geophys. J. Int.,* **113,** 399–418.

Gripp, A.E. & Gordon, R.G., 1990. Current plate velocities relative to the hotspots incorporating the NUVEL-1 global plate motion model, *Geophys. Res. Lett.,* **17,** 1109–1112.

Gripp, A.E. & Gordon, R.G., 2002. Young tracks of hotspots and current plate velocities, *Geophys. J. Int.,* **150,** 321–361.

Grunewald, S., Weber, M. & Kind, R., 2001. The upper mantle under Central Europe: Indications for the Eifel plume, *Geophys. J. Int.,* **147,** 590–601.

Grünthal, G. & Stromeyer, D., 1992. The recent crustal stress field in Central Europe: Trajectories and finite element modelling, *J. geophys. Res.,* **97,** 11 805–11 820.

Hartog, R. & Schwartz, S.Y., 2000. Subduction-induced strain in the upper mantle east of the Mendocino triple junction, California, *J. geophys. Res.,* **105,** 7909–7930.

Hirn, A., 1977. Anisotropy in the continental upper mantle: Possible evidence from explosion seismology, *Geophys. J. R. astr. Soc.,* **49,** 49–58.

Illies, J.H., Prodehl, C., Schmincke, H.-U. & Semmel, A., 1979. The Quaternary uplift of the Rhenish shield in Germany, *Tectonophysics,* **61,** 197–225.

Jung, S. & Hoernes, S., 2000. The major- and trace element and isotope (Sr, Nd, O) geochemistry of Cenozoic alkaline rift-type volcanic rocks from the Rhön area (central Germany): Petrology, mantle source characteristics and implications for asthenosphere-lithosphere interactions, *J. Volc. Geotherm. Res.,* **99,** 27–53.

Kaminski, E. & Ribe, N., 2002. Timescales for the evolution of seismic anisotropy in mantle flow, G^3, **3,** 1051–1068, doi:10.1029/2001GC000222.

Karato, S., 1989. Seismic anisotropy; mechanisms and tectonic implications, in *Rheology of Solids and of the Earth,* pp. 393–422, eds Karato, S. & Toriumi, M., Oxford Univ. Press, Oxford.

Karato, S.I., 2003. Mapping water content in the upper mantle, in *Inside the Subduction Factory, Geophysical Monograph 138,* pp. 135–132, ed. Eiler, J., Am. geophys. Un., Washington, DC.

Karato, S.I. & Wu, P., 1993. Rheology of the upper mantle: A synthesis, *Science,* **260,** 771–778.

Kendall, J.-M., 1994. Teleseismic arrivals at a mid-ocean ridge: Effects of mantle melt and anisotropy, *Geophys. Res. Lett.,* **21,** 301–304.

Keyser, M., Ritter, J.R.R. & Jordan, M., 2002. 3D shear-wave velocity structure of the Eifel plume, Germany, *Earth planet. Sci. Lett.,* **203,** 59–82.

Kumazawa, M. & Anderson, O.L., 1969. Elastic moduli, pressure derivatives, and temperature derivatives of single-crystal olivine and single-crystal forsterite, *J. geophys. Res.,* **74,** 5961–5972.

Laubscher, H.P., 1970. Grundsätzliches zur Tektonik des Rhein Graben, in *Graben Problems. Int. Upper. Mantle Project,* Vol. 27, pp. 79–86, eds Illies, J.H. & Müller, S., Sci. Rep, Schweizerbart, Stuttgart.

Leibecker, J., Gatzemeier, A., Honig, M., Kuras, O. & Soyer, W., 2002. Evidence of electrical anisotropic structures in the lower crust and upper mantle beneath the Rhenish Shield, *Earth planet. Sci. Lett.,* **202,** 289–302.

Lippolt, H.J., 1983. Distribution of volcanis activity in space and time, in *Plateau Uplift. The Rhenish Shield–A Case History,* pp. 112–120, eds Fuchs, K., von Gehlen, K., Mälzer, H., Muranski, H. & Semmel, A., Springer, Berlin.

McKenzie, D., 1979. Finite deformation during fluid flow, *Geophys. J. R. astr. Soc.,* **99,** 13 655–13 665.

Mainprice, D. & Silver, P.G., 1993. Interpretation of SK*S*-waves using samples from the subcontinental lithosphere, *Phys. Earth planet. Inter.,* **78,** 257–280.

Mendenhall, W. & Sincich, T., 1995. *Statistics for Engineering and the Sciences,* Prentice-Hall, Upper Saddle River, NJ.

Mercier, J.-C.C. & Nicolas, A., 1975. Textures and fabrics of upper-mantle peridotites as illustrated by xenoliths from basalts, *J. Petrol.,* **16,** 454–487.

Mertes, H. & Schmincke, H.-U., 1983. Age distribution of volcanoes in the West-Eifel, *N. Jahrb. Geol. Paläontol. Abh.,* **166,** 260–293.

Meyer, R., 2001. Teleseismische P-Wellendämpfung in der Eifel: Analyse und Tomographie, *PhD thesis*, Institute for Geophysics, University of Göttingen.

Milne-Thomson, L.M., 1968. *Theoretical Hydrodynamics,* 5th edn, pp. 211–213, Macmillan, New York.

Montagner, J.-P., 1994. What can seismology tell us about mantle convection?, *Rev. Geophys.,* **32,** 115–137.

Montagner, J.P. & Guillot, L., 2000. Seismic anisotropy in the Earth's Mantle, in *Problems in Geophysics for the Next Millenium,* pp. 218–253, eds Boschi, E., Ekström, G. & Morelli, A., Editrice Compostri, Bologna, Italy.

Montagner, J.-P., Griot, D.-A. & Lave, J., 2000. How to relate body wave and surface wave anisotropies?, *J. geophys. Res.,* **105,** 19 015–19 028.

Montelli, R., Nolet, G., Dahlen, F.A., Masters, G., Engdah, E.R. & Hung, S.H., 2004. Finite-frequency tomography reveals a variety of plumes in the mantle, *Science,* **303,** 338–343.

Moore, W.B., Schubert, G. & Tackley, P., 1998. Three-dimensional simulations of plume–lithosphere interaction at the Hawaiian swell, *Science,* **279,** 1008–1011.

Mueller, B., Wehrle, V., Zeyen, H. & Fuchs, K., 1997. Short-scale variations of tectonic regimes in the western European stress province north of the Alps and Pyrenees, *Tectonophysics,* **275,** 199–219.

Nicolas, A. & Christensen, N.I., 1987. Formation of anisotropy in upper mantle peridotites - A review, in *Composition, Structure and Dynamics of the Lithosphere–Asthenosphere System,* Vol. 16, pp. 111–123, eds Fuchs, K. & Froidevaux, C., Geodynamics Series, Am. geophys. Un., Washington DC.

Nicolas, A. & Poirier, J.P., 1976. *Crystalline Plasticity and Solid State Flow in Metamorphic Rocks,* John Wiley, New York, NY.

Olson, P., 1990. Hot spots, swells and mantle plumes, in *Magma Transport and Storage,* pp. 33–51, ed. Ryan, M.P., John Wiley, New York, NY.

Panza, G.F., Mueller, S. & Calcagnile, G., 1980. The gross features of the lithosphere–asthenosphere system in Europe from seismic surface waves and body waves, *Pure appl. Geophys.,* **118,** 1209–1213.

Passier, M.L. & Snieder, R.K., 1996. Correlation between shear wave upper mantle structure and tectonic surface expressions: Application to central and southern Germany, *J. geophys. Res.,* **101,** 25 293–25 304.

Ribe, N., 1992. On the relation between seismic anisotropy and finite strain, *J. geophys. Res.,* **97,** 8737–8747.

Ribe, N.M. & Christensen, U.R., 1994. Three-dimensional modelling of a mantle plume interacting with a moving plate, *J. geophys. Res.,* **99,** 669–682.

Ribe, N. & Christensen, U., 1999. The dynamical origin of Hawaiian volcanism, *Earth planet. Sci. Lett.,* **171,** 517–531.

Ribe, N. & Yu, 1991. A theory for plastic deformation and textural evolution of olivine polycrystals, *J. geophys. Res.,* **96,** 8325–8335.

Richards, M.A., Hager, B.H. & Sleep, N.H., 1988. Dynamically supported geoid highs over hotspots: Observation and theory, *J. geophys. Res.,* **93,** 7690–7780.

Ritsema, J. & Allen, R.M., 2003. The elusive mantle plume, *Earth planet. Sci. Lett.,* **207,** 1–12.

Ritter, J.R.R., 2005. Small-scale mantle plumes: Imaging and geodynamic aspects, in *Perspectives in Modern Seismology, Lecture Notes in Earth Sciences,* 105, pp. 69–94 eds Wenzel, F. & Fuchs, K., Springer-Verlag, Berlin.

Ritter, J.R.R., Achauer, U., Christensen, U.R. & the Eifel Plume Team, 2000. The teleseismic tomography experiment in the Eifel region, Central Europe: Design and first results, *Seism. Res. Lett.,* **71,** 437–443.

Ritter, J.R.R., Jordan, M., Christensen, U.R. & Achauer, U., 2001. A mantle plume below the Eifel volcanic fields, Germany, *Earth planet. Sci. Lett.,* **186,** 7–14.

Rümpker, G. & Ryberg, T., 2000. New 'Fresnel-zone' estimates for shear-wave splitting observations from finite-difference modelling, *Geophys. Res. Lett.,* **27,** 2005–2008.

Rümpker, G. & Silver, P.G., 1998. Apparent shear-wave splitting parameters in the presence of vertically varying anisotropy, *Geophys. J. Int.,* **135,** 790–800.

Rümpker, G. & Silver, P.G., 2000. Calculating splitting parameters for plume-type anisotropic structures of the upper mantle, *Geophys. J. Int.,* **143,** 507–520.

Russo, R.M. & Okal, E.A., 1998. Shear wave splitting and upper mantle deformation in French Polynesia: Evidence for small-scale heterogeneity related to the Society hotspot, *J. geophys. Res.,* **103,** 15 089–15 107.

Saltzer, R.L., Gaherty, J.B. & Jordan, T.H., 2000. How are vertical shear wave splitting measurements affected by variations in the orientation of azimuthal anisotropy with depth?, *Geophys. J. Int.,* **141,** 374–390.

Savage, M.K., 1998, Lower crustal anisotropy or dipping boundaries? Effects on receiver functions and a case study in New Zealand, *J. geophys. Res.,* **103,** 15 069–15 087.

Savage, M.K. & Sheehan, A.F., 2000. Seismic anisotropy and mantle flow from the Great Basin to the Great Plains, western United States, *J. geophys. Res.,* **105,** 13 715–13 734.

Silver, P.G., 1996. Seismic anisotropy beneath the continents: Probing the depths of geology, *Ann. Rev. Earth Planet. Sci,* **24,** 385–432.

Silver, P.G. & Chan, W.W., 1988. Implications for continental structure and evolution from seismic anisotropy, *Nature,* **335,** 34–39.

Silver, P.G. & Chan, W.W., 1991. Shear-wave splitting and subcontinental mantle deformation, *J. geophys. Res.* **96,** 16 429–16 454.

Silver, P.G. & Savage, M.K., 1994. The interpretation of shear-wave splitting parameters in the presence of two anisotropic layers, *Geophys. J. Int.,* **119,** 949–963.

Sittler, C., 1969. The sedimentary trough of the Rhine Graben, *Tectonophysics,* **8,** 543–560.

Sleep, N.H., 1987. Lithospheric heating by mantle plumes, *Geophys. J. R. astr. Soc.,* **91,** 1–12.

Sleep, N., 1990. Hotspots and mantle plumes: Some phenomenology, *J. geophys. Res.,* **95,** 6715–6736.

Smith, G.P. & Ekström, G., 1999. A global study of Pn anisotropy beneath continents, *J. geophys. Res.,* **104,** 963–980.

Turcotte, D.L. & Emerman, S.H., 1983. Mechanisms of active and passive rifting, *Tectonophysics,* **94,** 39–50.

Vinnik, L.P., Farra, V. & Romanowicz, B., 1989. Azimuthal anisotropy in the Earth from observations of SKS at Geoscope and NARS broadband stations, *Bull. seism. Soc. Am.,* **79,** 1542–1558.

Vinnik, L.P., Makeyeva, L.I., Milev, A. & Usenko, A.Yu., 1992. Global patterns of azimuthal anisotropy and deformations in the continental mantle, *Geophys. J. Int.,* **111,** 433–447.

Vinnik, L.P., Krishna, V.G., Kind, R., Bormann, P. & Stammler, K., 1994. Shear-wave splitting in the records of the German Regional Seismic Network, *Geophys. Res. Lett.,* **21,** 457–460.

Vinnik, L.P., Montagner, J.-P., Girardin, N., Dricker, I. & Saul, J., 2003. Comment on 'Shear-wave splitting to test mantle deformation models around Hawaii' by Kristoffer T. Walker, Götz H. R. Bokelmann & Simon L. Klemperer, *Geophys. Res. Lett.,* **30,** 1676, doi:10.1029/2002GL016712.

Walker, K.T., 2004. Exploring problems in tectonics and geodynamics with seismology, *PhD thesis,* Stanford University, Stanford, CA.

Walker, K.T., Bokelmann, G.H.R. & Klemperer, S.L., 2001. Shear-wave splitting to test mantle deformation models around Hawaii, *Geophys. Res. Lett.,* **28,** 4319–4322.

Walker, K.T., Bokelmann, G.H.R. & Klemperer, S.L., 2003. Reply to Comment by Vinnik, L.P., Montagner, J.P., Giradin, N., Dricker, I. & Saul, J., *Geophys. Res. Lett.,* **28,** 1676, doi:10.1029/2002GL016712.

Walker, K.T., Bokelmann, G.H.R. & Klemperer, S.L., 2004a. Shear-wave splitting beneath the Snake River Plain suggests a mantle upwelling beneath eastern Nevada, USA, *Earth planet. Sci. Lett.,* **222,** 529–542.

Walker, K.T., Nyblade, A., Klemperer, S.L., Bokelmann, G.H.R. & Owens, T., 2004b, On the relationship between extension and anisotropy: constraints from shear-wave splitting across the East African Plateau, *J. geophys. Res.,* **109,** B08302, doi:10.1029/2003JB002866.

Walker, K.T., Bokelmann, G.H.R., Klemperer, S.L. & Nyblade, A., 2005. Shear-wave splitting around hotspots: Evidence for upwelling-related mantle flow?, in *Plates, Plumes & Paradigms,* eds Foulger, G., Natland, J., Presnall, D. & Anderson, D., Geol. Soc. Am. Special Paper, **388,** 171–192.

Wilson, M. & Bianchini, G., 1999. Tertiary-Quaternary magmatism within the Mediterranean and surrounding regions, in *The Mediterranean Basins: Tertiary extension within the Alpine orogen,* Vol. 156, pp. 141–168, eds Durand, B., Jolivet, L., Horvath, F. & Seranne, M., Geol. Soc. Lond. Special Publication.

Wilson, M. & Downes, H., 1992. Mafic alkaline magmatism in the European Cenozoic rift system, Tectonophysics, **208,** 173–182.

Wilson, M. & Patterson, R., 2001. Intraplate magmatism related to short-wavelength convective instabilities in the upper mantle: Evidence from the Tertiary-Quaternary volcanic province of western and central Europe, in *Mantle Plumes: Their Identification Through Time,* Vol. 352, pp. 37–58, eds Ernst, R.E. & Buchan, K.L., Geol. Soc. Am. Special Paper.

Wolfe, C.J. & Silver, P.G., 1998. Seismic anisotropy of oceanic upper mantle; shear-wave splitting methodologies and observations, *J. geophys. Res.,* **103,** 749–771.

Wolfe, C.J. & Solomon, S.C., 1998. Shear-wave splitting and implications for mantle flow beneath the MELT region of the East Pacific Rise, *Science,* **280,** 1230–1232.

Wolfe, C.J., Bjarnason, G.C., VanDecar, J.C. & Solomon, S.C., 2002. Assessing the depth resolution of tomographic models of upper mantle structure beneath Iceland, *Geophys. Res. Lett.,* **29,** 1015–1018, doi: 10.1029/2001GL013657.

Wylegalla, K., Bock, G., Gossler, J., Hanka, W. & the TOR Working Group, 1999. Anisotropy across the Sorgenfrei-Tornquist Zone from shear wave splitting, *Tectonophysics,* **314,** 335–350.

Yanovskaya, T.B., Panza, G.F., Ditmar, P.D., Suhadolc, P. & Mueller, S., 1990. Structural heterogeneity and anisotropy based on 2-D phase velocity patterns of Rayleigh waves in Western Europe, *Atti Accad. Naz. Lincei Cl. Sci. Fis., Mat. Nat. Rend.,* **9,** 127–135.

Ziegler, P.A., 1992. European Cenozoic rift system, *Tectonophysics,* **208,** 91–111.

SUPPLEMENTARY MATERIAL

A supplementary appendix is available for this article online. It includes Tables S1 to S5 and Figs S1 and S2.

This material is available as part of the online article from http://www.blackwell-synergy.com